

# Biomolecule-functionalized exfoliated-graphene and graphene oxide as heteronucleants of nanocrystalline apatites to make hybrid nanocomposites with tailored mechanical, luminescent, and biological properties

Francisco Javier Acebedo-Martínez<sup>a,\*</sup>, Paula Alejandra Baldián<sup>b</sup>, Francesca Oltolina<sup>c</sup>,  
 Antonia Follenzi<sup>c</sup>, Giuseppe Falini<sup>d</sup>, Jorge Fernando Fernández-Sánchez<sup>e</sup>,  
 Duane Choquesillo-Lazarte<sup>a</sup>, Jaime Gómez-Morales<sup>a,\*</sup>

<sup>a</sup> Laboratory of Crystallographic Studies, IACT-CSIC, Avda. Las Palmeras, 4, E-18100, Armilla, Spain

<sup>b</sup> Department of Oral Health, Faculty of Odontology, Universidad Nacional de Colombia. Cra 30 No. 45-03, Ed. 210. Bogotá, Colombia

<sup>c</sup> Dipartimento di Scienze Della Salute, Università Del Piemonte Orientale A. Avogadro, Via Solaroli, 17, 28100, Novara, Italy

<sup>d</sup> Dipartimento di Chimica "Giacomo Ciamician", Alma Mater Studiorum Università di Bologna, Via Selmi 2, 40126, Bologna, Italy

<sup>e</sup> Department of Analytical Chemistry, Faculty of Sciences, University of Granada, Avda. Fuentenueva s/n, 18071, Granada, Spain

## ARTICLE INFO

Handling Editor: P. Vincenzini

### Keywords:

Graphene flakes  
 Graphene oxide  
 Nanocrystalline apatite  
 Biomolecules functionalization  
 Terbium  
 Nanocomposites

## ABSTRACT

Nanocrystalline apatite (Ap), known for its exceptional biological properties, faces limitations in hard tissue engineering due to its poor mechanical properties. To overcome this limitation, we investigated the preparation of nanocomposites through heterogeneous nucleation of calcium phosphate on exfoliated graphene (G) and graphene oxide (GO) flakes, selected for their outstanding mechanical properties. The flakes were treated (functionalized) with amino acids of varying isoelectric points—namely L-Arginine (Arg), L-Alanine (Aln) and L-Aspartic acid (Asp)—as well as citrate (Cit) molecules. Furthermore, Tb<sup>3+</sup> was incorporated into the formulations to introduce luminescence and further enrich the functionality of the composite. The synthesis was conducted using the sitting drop vapor diffusion method. Functionalized GO/Ap nanocomposites significantly improved roughness, adhesion forces and elastic modulus compared to Ap and G-based particles. GO-Asp-Ap-Tb nanocomposites exhibited the highest roughness ( $163.8 \pm 116.2$  nm), while G-Cit-Ap had the lowest ( $6.8 \pm 5.6$  nm). In terms of adhesion force, GO-Cit-Ap-Tb reached the highest value ( $31.06 \pm 13.3$  nN), while G-Arg-Ap had the lowest ( $3.7 \pm 1.8$  nN) compared to Ap ( $13.6 \pm 3.2$  nN). For the elastic modulus, GO-Aln-Ap-Tb demonstrated the greatest stiffness ( $3489 \pm 101.01$  MPa) compared to Ap ( $30.2 \pm 6.5$  MPa), while G-Aln-Ap-Tb showed the lowest ( $17.2 \pm 8.4$  MPa). Concerning their luminescence, regardless of G/Ap and GO/Ap, the relative luminescence intensities depended on the biomolecule used and decreased in the order Arg > Aln > Asp and Cit. Furthermore, G/Ap and GO/Ap nanocomposites demonstrated good biocompatibility on murine mesenchymal stem cells at low concentrations, showing cell viabilities exceeding 80 % at 0.1 µg/mL. This research offers a novel approach to enhancing the mechanical properties of apatites while preserving their good biocompatibility properties and introducing new functionalities (i.e. luminescence) in the composites, thereby expanding their range of applications in hard tissue engineering.

## 1. Introduction

Nanocrystalline apatites (nAp) are the primary mineral components of human bones and teeth [1]. These plate-shaped nonstoichiometric hydroxyapatite crystals are deficient in Ca<sup>2+</sup> and OH<sup>-</sup> and contain substituting ions such as CO<sub>3</sub><sup>2-</sup>, Mg<sup>2+</sup>, Na<sup>+</sup>, and others within their

crystal structure. Additionally, bone nAp are found coated by citrate molecules (Cit) [2], which are thought to play a crucial role in the formation, shaping, and hydrophobicity of the crystals during bone mineralization [3–5]. In fact, around 80 % of Cit present in the human body is found in bones [6,7]. Besides citrates, these crystals possess a non-apatitic hydrated surface layer, which imparts excellent surface ion

\* Corresponding author.

\*\* Corresponding author.

E-mail addresses: [j.acebedo@csic.es](mailto:j.acebedo@csic.es) (F.J. Acebedo-Martínez), [jaime@lec.csic.es](mailto:jaime@lec.csic.es) (J. Gómez-Morales).

<https://doi.org/10.1016/j.ceramint.2024.10.034>

Received 13 June 2024; Received in revised form 23 September 2024; Accepted 5 October 2024

Available online 8 October 2024

0272-8842/© 2024 The Authors. Published by Elsevier Ltd. This is an open access article under the CC BY-NC-ND license (<http://creativecommons.org/licenses/by-nc-nd/4.0/>).

exchange and adsorption capabilities. This hydrated layer is believed to be essential for homeostasis and other regulatory processes, including bone remodeling [8–10].

Similar to biological nAp, synthetic nAp exhibits excellent bioactivity and biocompatibility, as well as a lack of toxicity, inflammatory, or immune responses, and high bioresorbability. These properties make synthetic nAp highly valuable for applications in hard tissue engineering, biomedicine and drug delivery systems [11–13]. One of its primary uses in hard tissue engineering is the coating of implants and biomaterials, where the formation of a biomimetic nAp layer, enhances the integration and interaction processes, ultimately improving the biological performance of the biomaterial and promoting bone regeneration [14–17].

Despite their exceptional biological properties, nAp exhibits poor mechanical characteristics, resembling brittle foam, with low toughness and flexural strength. These limitations have hindered their broader use in the biomedical and pharmaceutical applications [18,19]. To address this challenge, composite formation has gained significant attention as an effective strategy. This approach enables the combination of the biological properties of nAp with a reinforcement material to enhance its mechanical performance [20,21]. Composites are created by integrating two or more constituent materials, resulting in a hybrid material that possesses enhanced properties from each component, which can be utilized across various fields, i.e. photocatalysis, environmental remediation, healthcare [22–28].

Graphene is a single layer of carbon atoms bonded together through  $sp^2$  hybridization [29], known for its exceptional mechanical properties [30]. Additionally, graphene and its derivatives graphene oxide (GO) and reduced graphene oxide (rGO), have demonstrated good biocompatibility, which is essential for their biomedical applications [31]. These qualities have positioned graphene and its derived materials as stand-out reinforcement material in CaP-composites [28,32–34].

Various methods have been reported for preparing composites of graphene and graphene oxide with CaPs, including *in situ* mineralization and hydrothermal synthesis, biomimetic mineralization, chemical vapor deposition, and electrochemical deposition [35–40]. In our study, we will explore the sitting drop vapor diffusion micro-method (SDVD), as reported in previous works [41–43], to induce the heterogeneous nucleation and growth of bone-like nAp particles on exfoliated graphene flakes (G, multilayer), prepared via sonication-assisted liquid-phase exfoliation (LPE) [44], as well as on commercial GO sheets. The goal is to obtain G/nAp and GO/nAp nanocomposites with improved mechanical performance compared to apatite alone. To enhance the biocompatibility of the nanocomposites, L-arginine (Arg), L-alanine (Aln), L-aspartic acid (Asp) and Cit (Fig. 1) will be incorporated in the LPE process of graphite and during the equilibration of GO suspensions.

The role of these amino acids, with isoelectric points (i.e.p) ranging from basic to acidic, — Arg (i.e.p = 10.76), Aln, (i.e.p = 6.00), Asp (i.e.p = 2.77) as well as Cit (citric acid  $pK_1 = 3.13$ ,  $pK_2 = 4.76$  and  $pK_3 = 6.40$ ) — has been previously studied in the control of bone-like apatite precipitation [45,46]. In this study, we will investigate whether these biomolecules influence the formation and properties of the G/Ap and GO/Ap nanocomposites. They are expected to function as dispersing

surfactants, assisting the graphite LPE process during sonication, binding to the surfaces of the exfoliated flakes to prevent re-aggregation, and act as nucleation sites to induce CaP formation. Furthermore, Cit is known for its efficient adsorption onto the nAp surfaces, with several studies confirming its role in enhancing the biocompatibility of the biomaterials, making it a suitable biosurfactant for this process [47,48].  $Tb^{3+}$  ions will be also supplemented to the formulation, to produce Tb-doped G/Ap and GO/Ap, imparting luminescent properties and expanding their potential applications (i.e. bioimaging) [49].  $Tb^{3+}$  exhibits notable photoluminescence in the UV and near infrared regions, long luminescence lifetimes, and strong resistance to photobleaching [50]. Besides these features,  $Tb^{3+}$  has been reported to induce bactericidal activity when incorporated into poly (vinyl alcohol)–alginate hydrogels reinforced with rGO [51], or promoted adhesion and osteogenic differentiation of human mesenchymal stem cells when used to dope apatite-mineralized collagen fibrils [52,53]. Other studies have shown that low concentrations of  $Tb^{3+}$  in Tb-doped nAp retains the physicochemical and biological benefits of the nAp, whereas higher  $Tb^{3+}$  concentrations can be harmful to the organism [54,55]. A thorough characterization will be conducted to determine how the biomolecules and the presence of  $Tb^{3+}$  influence the physicochemical, mechanical, luminescent, and biocompatibility properties of the nanocomposites. Unlike previous studies on G/Ap and related carbon-derived composites, which primarily focused on improving mechanical properties and biocompatibility [28], or enhancing its antibacterial properties [56], this research aims to fabricate new G/nAp and GO/nAp composites with improved mechanical performance and tailored luminescence properties, while maintaining good biocompatibility.

## 2. Experimental section

### 2.1. Nanocomposites preparation

G flakes were prepared by LPE of graphite, assisted by sonication, using Arg, Aln, Asp and Cit as dispersing surfactants. For this, 10 mL of ultrapure  $H_2O$  (Milli-Q) along with 100 mg of graphite powder (Sigma-Aldrich, purity 99.99 %) and either 3.48 mg of Arg, 1.78 mg of Aln, 2.66 mg of Asp or 3.84 mg of Cit (Sigma-Aldrich, purity 99 %) were placed into 20 mL sealed vials. The suspensions were sonicated in an ice bath for 5 h followed by centrifugation at 3500 rpm for 5 min. The supernatant was collected and sonicated for an additional hour and followed by a second centrifugation for 5 min and at 3500 rpm. The supernatant was carefully removed with a micropipette and stored at 4 °C before the mineralization experiments. Similarly, GO suspensions (10 mL) were prepared by diluting 1 mL of concentrated GO (Sigma-Aldrich, 99.99 % purity) and either 3.48 mg of L-Arg, 1.78 mg of L-Aln, 2.66 mg of L-Asp or 3.84 mg of Cit, followed by 30 min of sonication.

The pH was measured two times: first, after preparing the G and GO suspensions and, second, after the mineralization stage. The mineralization of G and GO flakes was conducted using the SDVD method in a *crystallization mushroom* (Triana Sc. & Tech, S.L.) at 20 °C and 1 atm total pressure. Each mushroom contained 12 droplets of 40  $\mu$ L in the crystallization chamber. The droplets were prepared by mixing 20  $\mu$ L of

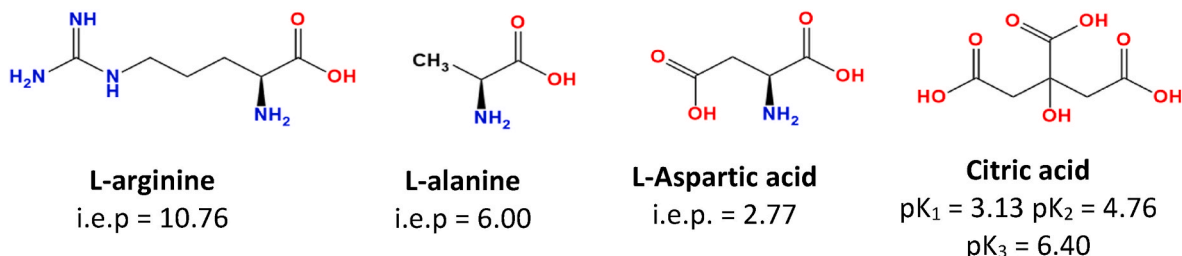


Fig. 1. Biomolecules used as surfactants for the graphite LPE process and functionalization of G and GO flakes.

either the G or GO suspensions with 50 mM  $\text{Ca}(\text{CH}_3\text{COO})_2$  and 20  $\mu\text{L}$  of 30 mM  $(\text{NH}_4)_2\text{HPO}_4$ , while the gas generation chamber held 3 mL of a 40 mM  $\text{NH}_4\text{HCO}_3$ . Control droplets without G or GO flakes were included in each mushroom as references. The crystallization chamber was sealed with the glass cover using high vacuum silicon grease and left undisturbed for 21 days. At the end of the experiments, the droplets were collected and transferred to an Eppendorf tube. After centrifugation at 10,000 rpm for 15 min, the supernatant was removed, and the final pellet was washed twice with 1 mL of ultrapure MilliQ water. Centrifugation was repeated to remove the supernatant and the final pellet was left to dry at 35 °C for 1 day.

## 2.2. Physico-chemical and morphological characterization

Powder X-ray diffraction (XRD) patterns were obtained with a Bruker D8 Advance Series II Vario diffractometer (Bruker AXS, Karlsruhe, Germany) equipped with a Ge (111) primary monochromator and a LynxEye fast silicon strip detector. Generator operating conditions were 40 kV and 40 mA, using  $\text{Cu K}\alpha$  radiation. Measurements were conducted in transmission geometry between Mylar foils with the beam focused on the detector.

Fourier transform infrared spectra (FTIR) were recorded in transmittance mode over a wavelength range of 4000  $\text{cm}^{-1}$  to 400  $\text{cm}^{-1}$  using a PerkinElmer Spectrum One FTIR spectrometer (PerkinElmer, Shelton, USA). Pellets were prepared by mixing 1 wt% sample with anhydrous KBr and pressing the mixture at 10 tons with a hydraulic press. Pure KBr pellets were used to record the background.

Raman spectra were recorded using a LabRAMHR spectrometer (Jobin-Yvon, Horiba, Tokyo, Japan). The excitation source was a diode laser emitting at a wavelength of 532 nm and detection was carried out using a Peltier-cooled charge-couple device (CCD) with a resolution of 1064 6256 pixels.

Crystal size distributions (CSD) and electrophoretic mobilities ( $\zeta$ -potentials) were measured using a Zetasizer Nano ZS analyzer (Malvern Instruments Ltd, Malvern, UK) in aqueous suspensions ( $\sim 0.5$  mg/mL, 25 °C) contained in disposable polystyrene cuvettes. For  $\zeta$ -potential measurements as a function of pH, a MPT-2 autotitrator (Malvern Instruments Ltd, Malvern, UK) was used to adjust the pH of the suspensions. Diluted HCl and NaOH solutions (0.25 and 0.1 M, respectively) were employed as titration reagents without any extra electrolyte.

The morphological features of G/nAp and GO/nAp nanocomposites were studied using scanning electron microscopy (SEM) and transmission electron microscopy (TEM). SEM was performed using a JEOL JSM 6490-LV scanning electron microscope (JEOL Inc., MA, USA) equipped with tungsten filament, operating at a voltage of 10 kV acceleration for secondary electron imaging (SEI) using an Everhart-Thornley detector and for backscattered electron detection. Before analysis, samples were dried in a JEOL EMDSC-U10A desiccator purge vacuum (JEOL Inc., MA, USA). Particle morphology was examined at 100x, 70,000x and 50,000x, and chemical analysis was conducted via energy dispersive X-ray spectroscopy (EDX).

Field emission scanning electron microscopy (FESEM) observations were carried out with a GEMINI LEO 1500 model Instrument (Zeiss, Jena, Germany). Samples were deposited on conventional supports, and then they were carbon-sputtered prior to observation. TEM observations were performed with a TEM Libra 120 Plus instrument operating at 80 kV (Carl Zeiss, Jena, Germany), equipped with Electron Energy Loss Spectroscopy (EELS) for microanalysis. Prior to TEM analysis, samples were dispersed in absolute ethanol ( $\geq 99.8$  % v/v) and deposited on copper microgrids coated with FORMVAR carbon film.

## 2.3. Mechanical properties

Surface roughness, adhesion force, and electric field gradient ( $\Delta V$ ) measurements were conducted in tapping mode, while the elastic nanomechanical properties of the particles were analyzed using force

spectroscopy mode with the Scanning Probe-Asylum Research 3D MFP BIO AFM equipment (Asylum Research, Santa Barbara, CA, USA). A silicon probe with a spherical apex of 30 nm was used along 224 scan lines and points, a scan rate of 0.80 Hz, and a scan size of 2.00  $\mu\text{m}$ . A compressive load of 10 nN was applied to induce elastic deformation of the particles, and force-distance curves were acquired using the Hertz model to quantitatively measure the surface elastic modulus. For each sample, deformation was assessed in a 10x10 point area, resulting in 100 points per sample. Data visualization and analysis were conducted using the modular program for Gwyddion scanning probe microscopy (Slashdot Media, San Diego, CA, USA). Results are reported as the means values, standard deviation, and Root Mean Square (RMS).

## 2.4. Luminescence properties

The luminescence characterizations of the powder materials, including luminescence spectra, luminescence lifetime ( $\tau$ ), and the relative luminescence intensities (R.L.I) was carried out using a Cary Eclipse Varian Fluorescence Spectrophotometer (Varian Australia, Mulgrave, Australia), using a front surface accessory. The instrumental parameters for characterizing the solid particles were:  $\lambda_{\text{exc}} = 375$  nm,  $\lambda_{\text{em}} = 545$  nm, slit-width<sub>exc/em</sub> = 10/10 nm, delay time ( $t_d$ ) = 120  $\mu\text{s}$ , gate time ( $t_g$ ) = 5 ms and detector voltage = 700 V. Luminescence lifetimes ( $\tau$ ) were measured using the following conditions:  $\lambda_{\text{exc/em}} = 375/545$  nm, slit-width<sub>exc/em</sub> = 20/20 nm,  $t_d = 100$   $\mu\text{s}$ ,  $t_g = 0.1$  ms and detector voltage = 800 V.

The fluorescence of the functionalized particles was characterized with an Olympus IX81 scanning confocal microscope (BioTek Instruments, Charlotte, VT, USA). This microscope enables high-quality fluorescence measurements as a function of the distance from the focal plane. Scan were performed at two wavelengths: blue channel (405 nm excitation/412 nm–476 nm emission), and the red channel (559 nm excitation/575 nm–615 nm emission), with 2  $\mu\text{m}$  increments to capture images of fluorescence across different wavelength detection channels. Mean fluorescence intensity (MFI) was calculated based on the maximum intensity projections of the confocal stacks.

## 2.5. Biological properties

The biocompatibility of the different nanocomposites was evaluated using m17.ASC cells, firstly described by Zamperone et al. as an immortalized mouse mesenchymal stem cell clone derived from subcutaneous adipose tissue. Cells were cultured in Claycomb medium with 2 mM L-glutamine, an antibiotic solution (streptomycin 100  $\mu\text{g}/\text{mL}$  and penicillin 100 U/mL, Sigma-Aldrich), and 10 % foetal calf serum. Standard conditions for cells maintenance were 37 °C and 5 %  $\text{CO}_2$  with splitting at 80–90 % confluency at a ratio of 1:10, and the medium was replaced every two days. Following a 24-h incubation period, 100  $\mu\text{L}$  of each nanocomposite (at concentrations ranging from 0.1 to 100  $\mu\text{g mL}^{-1}$ ) were incubated with the cells.

Cell viability was assessed after three days of incubation using the MTT colorimetric assay (3-(4,5-Dimethylthiazol-2-yl)-2,5-diphenyltetrazolium bromide, Sigma-Aldrich, St. Louis, MO, USA). Each well was treated with 20  $\mu\text{L}$  of MTT solution (5 mg/mL in a PBS solution) and incubated for 2 h at 37 °C. Afterwards, once the formazan crystals have dried, a 0.2 M HCl acidified isopropanol solution was added to dissolve them. The optical density was measured at 570 nm using a multi-well reader (2030 Multilabel Reader Victor TM X4, PerkinElmer, Waltham, MA, USA). For each sample, four independent experiments were conducted in triplicate. Untreated cells were used as 100 % viability control while soluble doxorubicin (DOXO) was used as cytotoxicity internal control. Statistical analysis was performed using GraphPad Prism version 10.1.2 for Windows to conduct a one-way ANOVA with Dunnett's post-test (GraphPad Software, San Diego, CA, USA).

### 3. Results

#### 3.1. Physicochemical and morphological characterization

The process for synthesizing the nanocomposites is illustrated in Fig. 2. Initially, graphite was dispersed in water in the presence of Arg, Aln, Asp, and Cit using the LPE process, resulting in aqueous suspensions of G flakes (Fig. 2A). The pH of graphite suspensions before LPE was 5.23. Similarly, the GO suspensions (pH = 1.73) prepared with commercial GO flakes were sonicated in the presence of these biomolecules. The biomolecules affected the pH differently, i.e. G-Arg, 7.34; G-Aln, 6.24; G-Asp, 3.85; G-Cit, 3.30; GO-Arg, 3.94; GO-Aln, 3.15; GO-Asp 3.00, and GO-Cit, 3.10. Next, twelve 40-  $\mu$ L droplets containing the G and GO suspensions along with the Ca and P reagents in stoichiometric composition were introduced into the *crystallization mushrooms* to precipitate CaP by the SDVD method (Fig. 2B). In all experiments, the pH of the droplets increased due to  $\text{NH}_3$  diffusion, stabilizing around 8, the optimum pH for apatite formation [57]. The TEM images (Fig. 2C) reveal that nanosized apatite particles coated the flakes, with no apatite forming outside the flakes, indicating the nucleation was heterogeneous and induced by the biomolecules-functionalized flakes.

Fig. 2D displays representative XRD, Raman, and FTIR characterizations of the nanocomposites for the Cit case. XRD is commonly used for structural characterization of carbon-based materials [58]. The XRD patterns (Fig. 2Da) display the characteristic reflections of the Ap phase. These reflections are found at  $2\theta$  values of  $25.8^\circ$ ,  $31.77^\circ$ ,  $32.19^\circ$ ,  $32.9^\circ$ ,  $33.9^\circ$ ,  $35.48^\circ$ , and  $39.81^\circ$ , corresponding to the (002), (211), (112), (300), (202), (301), and (310) planes respectively (as indicated by apatite ASTM card file no. 9-432). Additionally, minor reflections, also associated with the Ap phase, can be seen in the  $2\theta$  range from  $40^\circ$  to  $45^\circ$ . No additional CaP phases such as octacalcium phosphate (OCP, ASTM card file no. 26-1056) or brushite (DCPD, ASTM card file no. 9-77) were found. This is evidenced by the absence of reflections at  $2\theta$   $4.8^\circ$  and  $11.6^\circ$ , which correspond to the (100) plane of OCP and the

(020) plane of DCPD, respectively. The XRD patterns of the nanocomposites prepared with amino acids and  $\text{Tb}^{3+}$  are shown in Figs. S1a, d, and g (see Supplementary Material). In the GO-Aln-Ap-Tb sample, an additional small reflection at  $2\theta = 29.5^\circ$  was identified as cubic terbium oxide (PDF card no. 00-019-1326). Furthermore, in all Tb-doped G-Ap samples, a small peak at  $2\theta = 26.51^\circ$  was observed, associated with the main reflection of graphite (PDF card no. 01-089-7213). This suggests that some graphite particles have remained in the suspension without exfoliating into G flakes. The broad Ap reflections in the diffractograms indicate the nano-scale dimensions of its crystalline domains, with average lengths of  $30 \pm 2$  nm.

Raman spectroscopy is a commonly used technique to characterize graphene and CaP materials [59]. The Raman spectra (Fig. 2 Db, and S1b, e, h) display the characteristic signals of the Ap at  $960\text{ cm}^{-1}$  ( $\nu_1\text{PO}_4$ ),  $428\text{ cm}^{-1}$  ( $\nu_2\text{PO}_4$ ),  $1043\text{ cm}^{-1}$  ( $\nu_3\text{PO}_4$ ) and  $586\text{ cm}^{-1}$  ( $\nu_4\text{PO}_4$ ). Additionally, the presence of  $\text{CO}_3$  ( $\nu_1\text{CO}_3$ ) signals at  $1069\text{ cm}^{-1}$  indicates the carbonation of the mineral, a key feature of biological apatites [60,61]. In G samples two bands are observed at 1465 and  $1526\text{ cm}^{-1}$ , corresponding to the D and G bands of the G flakes [62]. Similarly, GO samples present two prominent signals at 1358 and  $1601\text{ cm}^{-1}$ , representing the D and G bands of GO.

The complementary FTIR spectra confirm the presence of Ap in the nanocomposites (Fig. 2Dc and S1c, f, i), as indicated by an intense band at  $1000\text{--}1100\text{ cm}^{-1}$ , attributed to the asymmetric stretching mode of  $\text{PO}_4^{3-}$  groups ( $\nu_3\text{PO}_4$ ). A smaller band at  $\sim 958\text{--}960\text{ cm}^{-1}$  corresponds to the symmetric stretching ( $\nu_1\text{PO}_4$ ) mode. Additionally, less intense bands at 603 and  $562\text{ cm}^{-1}$  are associated with the bending mode of  $\text{PO}_4^{3-}$  groups ( $\nu_4\text{PO}_4$ ), while the band at  $467\text{--}470\text{ cm}^{-1}$  corresponds to the  $\nu_2\text{PO}_4$  vibration mode. Additionally, the presence of carbonate vibration modes at  $\sim 1414\text{ cm}^{-1}$  and  $1473\text{ cm}^{-1}$  ( $\nu_3\text{CO}_3$ ) along with a small peak around  $875\text{ cm}^{-1}$  ( $\nu_2\text{CO}_3$ ) confirm the incorporation of  $\text{CO}_3$  into the Ap structure. Table S1 shows the carbonation percentages of the nAp in the different composites, estimated following the quantification method proposed by Grunenwald et al. [63]. These values are consistently lower

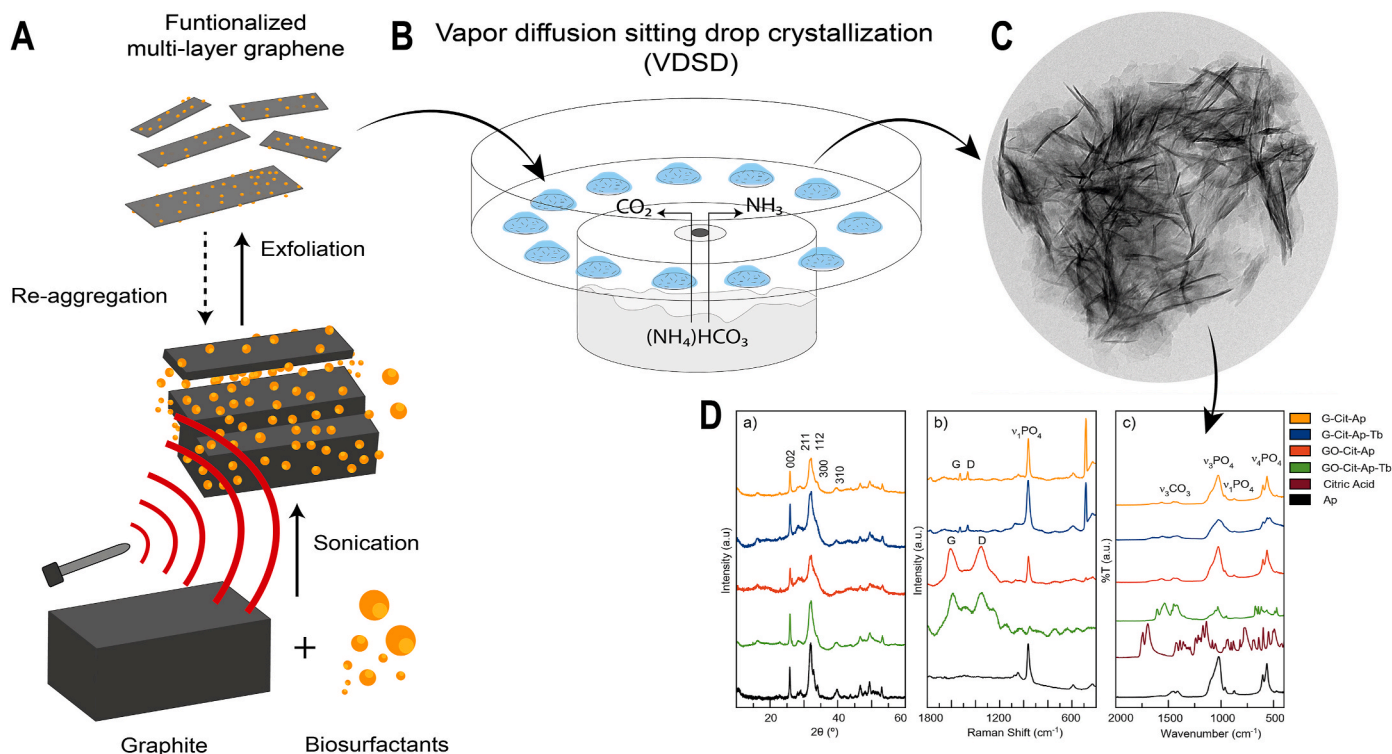


Fig. 2. Methodological set-up for the mineralization of G and GO flakes. A) Schematic diagram of sonication-assisted liquid phase exfoliation (LPE) of graphite. B) Schematic diagram of the VDSO crystallization method. C) TEM image of G-Cit-Ap nanocomposites. Da) XRD patterns, Db) Raman spectra, and Dc) FTIR spectra of Cit-derived nanocomposites.



than in pure nAp, but higher in the composites containing  $\text{Tb}^{3+}$  compared to those  $\text{Tb}^{3+}$ -free. The graphite spectra do not display any remarkable feature. However, the GO sample exhibits a broad peak at around  $3650\text{ cm}^{-1}$  (not shown) attributed to the O–H stretching, which is also slightly observed in its composites. Other minor bands of GO are present in the  $1730\text{--}1500\text{ cm}^{-1}$  and  $1060\text{--}850\text{ cm}^{-1}$  regions.

Additionally, several bands within the wavenumber range from  $1300\text{ cm}^{-1}$  to  $1700\text{ cm}^{-1}$  (Figs. S1c, f, i) correspond to symmetric/asymmetric stretches of  $\text{COO}^-$  and  $\text{NH}_2 \cdots \text{H}^+$  groups, at  $1400\text{--}1430/1560\text{--}1600\text{ cm}^{-1}$  and  $1550\text{--}1485/1590\text{--}1660\text{ cm}^{-1}$ , respectively, which are associated with chemisorbed amino acids [64–66]. These bands exhibit higher relative intensity compared to that of  $\text{PO}_4^{3-}$  bands in the Tb-doped GO/Ap composites and lower intensity in those without  $\text{Tb}^{3+}$ . In G/Ap nanocomposites, the relative intensity of these bands is very low, likely due to the intercalation of the biomolecules within the exfoliated G flakes during the LPE process. Taken together, these results confirm the successful mineralization of G and GO flakes with nAp possessing biomimetic features, using the VDS method.

The measurement of CSD and  $\zeta$ -potentials of G and GO suspensions can provide valuable insights into the ability of the biosurfactants to stabilize flakes before mineralization, as well as the stability of aqueous suspensions of the resulting nanocomposites. High absolute values of  $\zeta$ -potential indicate a strong repulsion and great colloidal stability, while values near zero are associated with aggregation or flocculation processes. The  $\zeta$ -potential data, collected across a pH range from 4.0 to 11.0, are shown in Fig. 3A. Both Exfoliated G and commercial GO exhibit negative  $\zeta$ -potentials with high absolute values, indicating that aqueous suspensions of the flakes (for G, after LPE) exhibit great stability at these pHs, effectively preventing re-aggregation. After the mineralization process, the nanocomposite suspensions exhibit a  $\zeta$ -potential closer to 0 across the entire pH range, particularly at physiological pHs ( $\sim 7.4$ ).

This indicates a tendency for particle aggregation and flocculation within the colloid. However, this behaviour is not problematic for the use of these nanocomposites as bone alloplasts. The effect of the additives was significant only in certain cases: Aln and Cit in G composites, Aln and Arg in GO composites, and Arg in Tb-doping GO composites when the pH was equal to or greater than 7.4. In the former cases, the  $\zeta$ -potentials notably decreased with increasing pH, whereas in the latter, they increased and even became positive in the same pH range, due to the higher  $\text{Tb}^{3+}$  content, causing the reversion of charge.

Regarding the influence of particle size on colloid stability, when particles are small enough, a high absolute  $\zeta$ -potential value is enough to confer stability; however, larger particle sizes negatively affect the stability of the suspensions [67,68]. Fig. 3B displays the cumulative volume-based distribution of the different nanocomposites as characterized by DLS. The percentiles  $D_{10}$ ,  $D_{50}$  and  $D_{90}$  (dashed horizontal lines) are clearly visible. These percentiles are widely used in the pharmaceutical industry to represent the sizes of a drug crystal population [69,70]. Each percentile represents the percentage of particles below a given size:  $D_{10}$  represents the size of smaller individual particles,  $D_{50}$  corresponds to the median of the distribution, and  $D_{90}$  provides information on nearly the entire population, mainly reflecting particle aggregation. In general, nanocomposites exhibit larger particle size and greater tendency to aggregate compared to non-mineralized G and GO flakes, consistent with the  $\zeta$ -potentials results. The GO nanocomposites exhibit higher values of  $D_{10}$ ,  $D_{50}$ , and  $D_{90}$  compared to those of G nanocomposites, indicating larger particle sizes and a greater tendency to aggregate. This behavior is attributed to increased mineralization induced by -OH and O-containing functional groups at the surface along to the adsorbed amino acids or Cit. Interestingly, this finding does not correlate with the isoelectric points of the amino acids that functionalize the surface of the flakes.

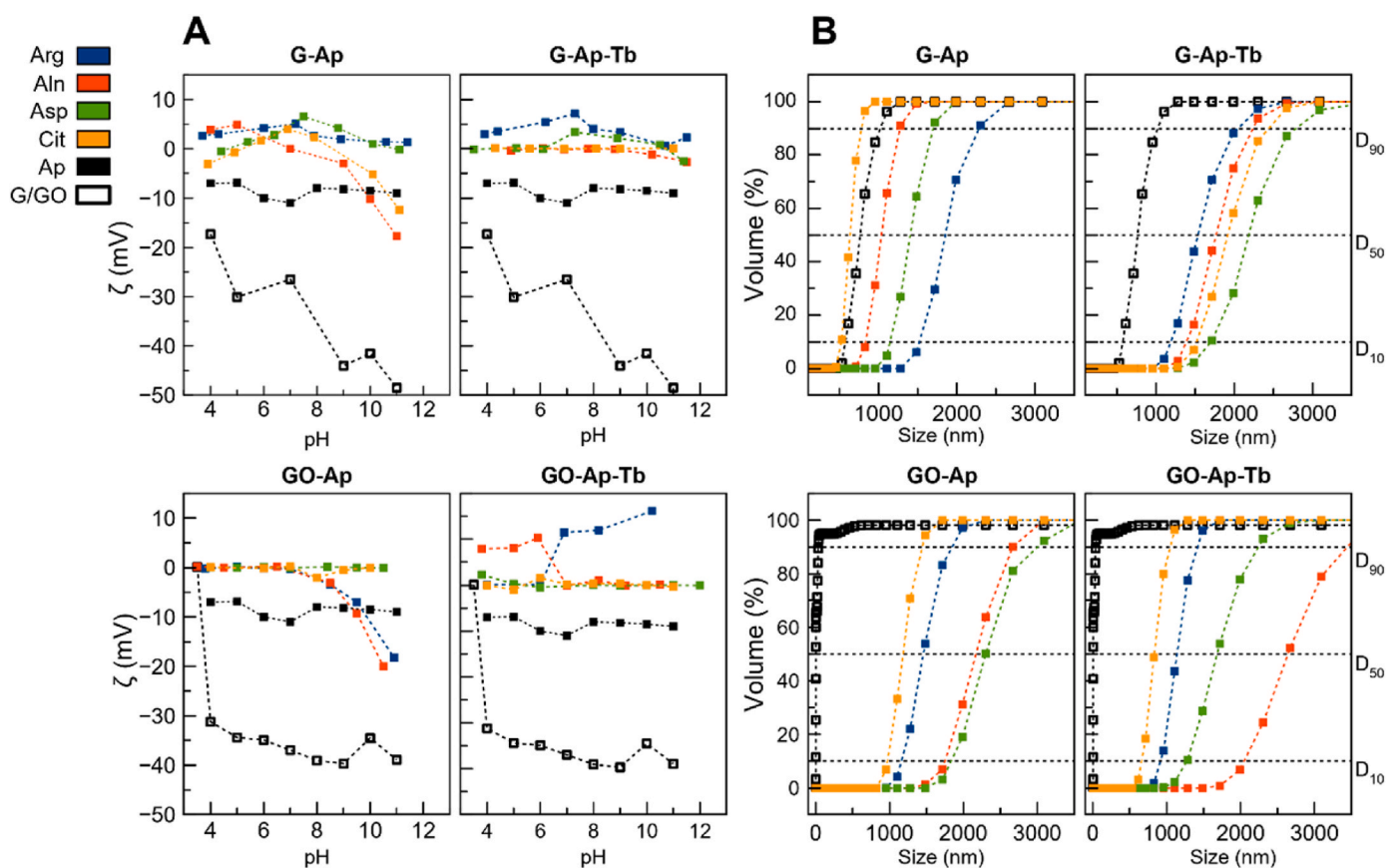


**Fig. 3.** A) Evolution of  $\zeta$ -potential of aqueous suspensions of the nanocomposites at pHs between 4.0 and 11.0. B) Cumulative volume-based distribution of the nanocomposites.

The morphological features of G/nAp and GO/nAp composites, after 3 weeks of mineralization, were characterized by SEM and TEM (Fig. 4, Fig. S2). SEM images (Fig. 4A, left columns) reveal the multilayer structure of the G sheets in G/nAp composites. GO flakes are also observed, though less distinct due to the thicker and more extensive Ap coating compared to G. This observation holds true for all GO nanocomposites and is attributed to the hydrophilic nature of the GO surface, which is populated of  $-OH$  and  $-COO^-$  functional groups at their surfaces, acting as additional binding sites for CaP nucleation.

TEM images (Fig. 4A, right columns) show the coating of the flakes with nAp with no particles observed outside the flakes, confirming the role of the flakes as heteronucleant surfaces. A focus to the crystals confirms their anisotropic nature, displaying thin hexagonal shapes with lengths of 50–60 nm and width of 6–10 nm. Aggregation of nAp was noted across all the samples and conditions, a phenomenon commonly seen in biological apatites [71]. Isolated G and GO flakes exhibited a range of sizes, from 30 to 350 nm, and showed irregular shapes. No significant differences were observed in the morphologies of nAp

crystals coating the flakes between samples prepared with the different amino acids and Cit; then the amino acids do not seem to significantly affect the morphology of the nAp, but indeed played a role for  $Tb^{3+}$  incorporation in the composites.

Elemental analysis of the nanocomposites by EDX (Table S2) revealed the presence of C, O, Ca and P (atom %) corresponding to G, GO and the apatite crystals coating both surfaces. In samples doped with  $Tb^{3+}$  the Tb content ranged from 1.1 to 1.8 atom % in G/nAp and from 1.3 to 3.3 atom % in GO/nAp composites, with the highest Tb content in GO-Arg-Tb-Ap composites. The Tb content showed a positive correlation with the isoelectric point of the amino acids. EDX mappings in Fig. 4B illustrates that Tb atoms are spread over the surface of the composite, with higher concentration observed in the apatite deposits, confirming successful doping of the nAp. On average, GO nanocomposites, contain between 8.8 and 10 atom% N, and between 6.7 and 9.0 atom% N in Tb-doped samples, attributed to the amino acids attached to the surfaces following sonication. In contrast, N was not detected by EDX in the G composites.

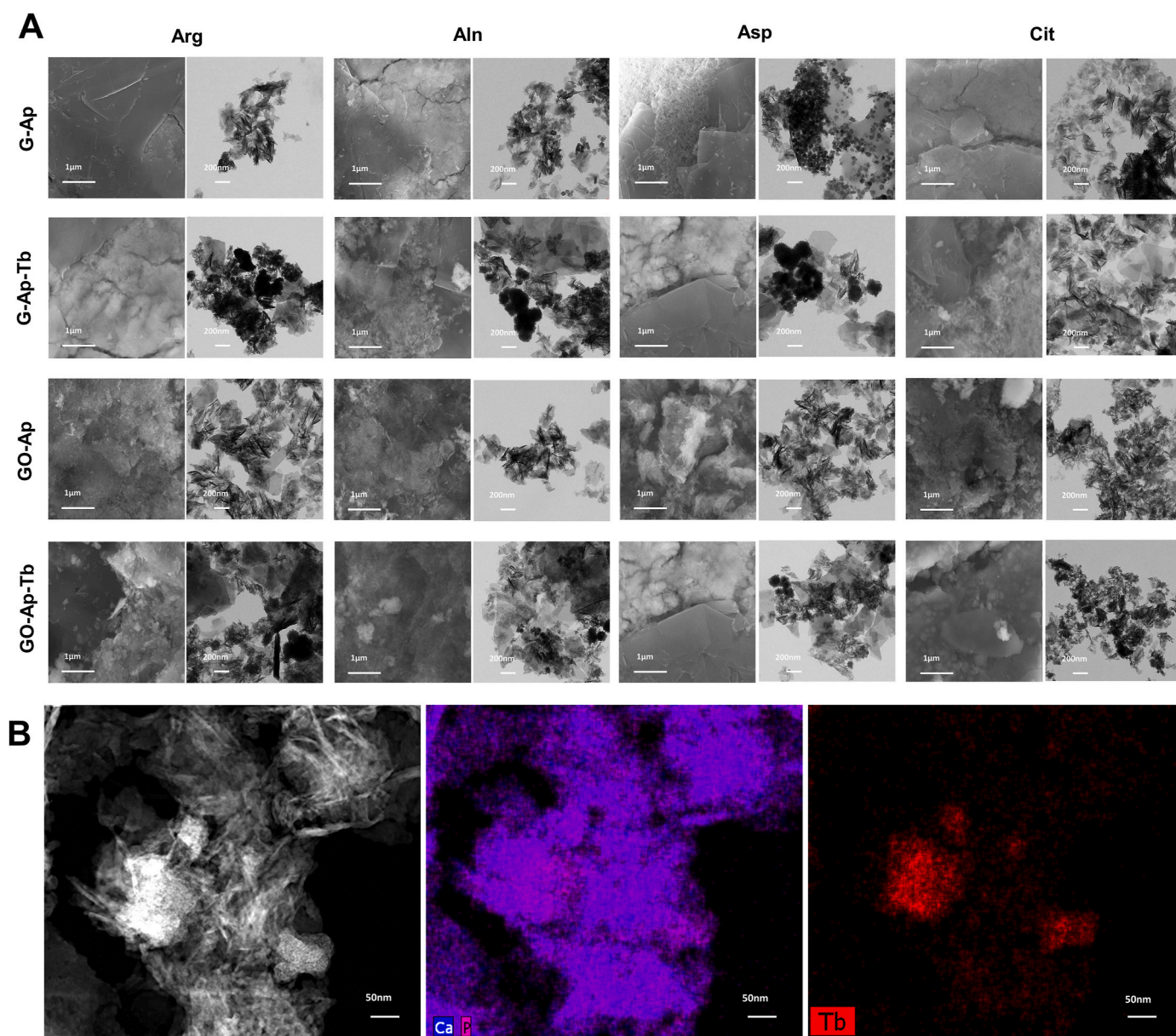


Fig. 4. A) Morphological and compositional features of the composites. Left column represents SEM images while right column represents TEM images B) HAADF-STEM micrograph and EDX mappings of the Ca, and Tb elemental analysis of G-Cit-Ap-Tb as representative.



### 3.2. Mechanical and surface properties of G/Ap and GO/Ap nanocomposites

Roughness, adhesion, and electrical properties of the functionalized particles were evaluated using AFM, which provides a 3D nanoscale profile. The force between the probe and the surface was measured to determine the  $\Delta V$ , adhesion force, and surface roughness.

The functionalized GO/Ap nanocomposites exhibit greater surface roughness compared to G/nAp particles, regardless of the amino acid used for functionalization of the flakes. The presence of  $Tb^{3+}$  further increased the surface roughness in both G/Ap and GO/Ap nanocomposites. The adhesion force of Ap was higher than that of the G/Ap and GO/Ap nanocomposites stabilized with Arg and Aln, whether  $Tb^{3+}$  was present or not. G/Ap particles stabilized with Asp displayed an adhesion force similar to Ap, while the highest adhesion values were obtained for GO-Ap particles stabilized with Asp and Cit, as well as in samples containing both amino acids and  $Tb^{3+}$ . On the other hand, the  $\Delta V$  decreases in both G-Ap and GO-Ap samples compared to Ap. Treatment with Aln, Asp and Cit led to an increase of  $\Delta V$ , which decreased in the presence of  $Tb^{3+}$ . GO/Ap composites, regardless of the stabilizing amino acid, exhibited lower  $\Delta V$ , but this value increased when  $Tb^{3+}$  was present (Tables 1 and 2).

Elastic deformation of the functionalized particles was also evaluated in the hybrid nanocomposites. The combination of G and GO with nAp to form the G/nAp and GO/nAp nanocomposites effectively increased the elastic modulus values of the composites compared to the Ap control. The Root Mean Square (RMS) values were calculated from 100 measured points per sample. The elastic modulus is reported in RMS since the data showed significant variations with extreme values for some of the composite particles, depending on the indented area on the particle's surface (Ap or G/GO) (Fig. 5). Typical values in the dataset for each sample are presented as the mean and standard deviation in Table 3. Based on RMS values, the composites with higher elastic modulus compared to Ap were GO-Arg-Ap-Tb, GO-Asp-Ap-Tb, GO-Cit-Ap, and G-Asp-Ap. When considering the average values, GO-Aln-Ap-Tb nanocomposites exhibited the highest elastic modulus.

### 3.3. G/Ap and GO/Ap luminescent properties

The luminescence properties in solid phase of Tb-doped G and GO nanocomposites in the solid phase are shown in Fig. 6. The sensitized luminescence excitation wavelengths are 350, 360 and 380 nm, with emission wavelengths at 490, 545, 585, 620 and 650 nm, similar to other lanthanides-doped nanomaterials [72,73]. It is well known that Tb-doped Ap can be excited at the CTB band (centred at 230 nm approximately). However, a longer excitation wavelength is preferred, as it produces the same emission spectra while enhancing biological applicability [74]. In fact, 375 nm (corresponding to the  $Tb^{3+} {}^7F_6 \rightarrow {}^5G_6, {}^5D_3$  transition) was selected as excitation wavelength. Regarding the

**Table 1**

Characterization of roughness, adhesion force and electrical parameters of G nanocomposites by atomic force microscopy.

Nanocomposite Type	Roughness (nm)	Adhesion force (nN)	Variation of electric potential (mW)
Ap	35.8 ± 28.9	13.6 ± 3.2	13936
G-Arg-Ap	28.8 ± 23.7	3.7 ± 1.8	74
G-Arg-Ap-Tb	33.1 ± 10.7	6.3 ± 4.2	69
G-Aln-Ap	13.1 ± 9.9	5.8 ± 2.9	890
G-Aln-Ap-Tb	38.9 ± 28.7	7.6 ± 3.7	39.8
G-Asp-Ap	8.1 ± 6.1	14.8 ± 5.4	1358
G-Asp-Ap-Tb	23.3 ± 18.4	8.02 ± 6.5	32
G-Cit-Ap	6.8 ± 5.6	7.7 ± 3.2	1600
G-Cit-Ap-Tb	15.8 ± 10.5	8.6 ± 3.2	19.8

\* Roughness RMS: Root Mean Square (the absolute root mean square values of the surface roughness profile).

**Table 2**

Characterization of roughness, adhesion force and electrical parameters of GO nanocomposites by atomic force microscopy.

Nanocomposite Type	Roughness (nm)	Adhesion force (nN)	Variation of electric potential (mW)
Ap	35.8 ± 28.9	13.6 ± 3.2	13936
GO-Arg-Ap	120.4 ± 95.8	4.4 ± 3.1	147.6
GO-Arg-Ap-Tb	127.4 ± 97.3	6.2 ± 4.2	367
GO-Aln-Ap	41.1 ± 27.5	6.2 ± 16.3	16.52
GO-Aln-Ap-Tb	118.9 ± 99.1	10.2 ± 4.7	105.6
GO-Asp-Ap	133.5 ± 109.6	16.1 ± 6.2	110
GO-Asp-Ap-Tb	163.8 ± 116.2	21.5 ± 11.2	426
GO-Cit-Ap	105.2 ± 23.6	20.6 ± 10.1	21.2
GO-Cit-Ap-Tb	116.4 ± 90.8	31.06 ± 13.3	310

\* Roughness RMS: Root Mean Square (the absolute root mean square values of the surface roughness profile).

emission wavelength, the one that produces the highest relative luminescence intensity (R.L.I.) corresponds to the hypersensitive transition without an inversion center ( ${}^5D_4 \rightarrow {}^7F_5$ ), consistent with other Tb-doped nanomaterials [75] (Fig. 6A<sub>1</sub>, A<sub>2</sub>).

In comparing the R.L.I. in Tb-doped G/Ap (Fig. 6 B<sub>1</sub>) and Tb-doped GO/Ap composite particles (Fig. 6 B<sub>2</sub>), it is clear that Tb-free materials show no luminescent emission, or only residual emission. This confirms that the luminescence is solely due to the presence of  $Tb^{3+}$ . The highest R.L.I. in both types of nanocomposites is achieved when Arg is used followed by Aln, Asp, and Cit, which correlates with the  $Tb^{3+}$  content (Table S2) and the i.e.p. of the amino acids. Moreover, there are no significant differences in R.L.I. between G and GO samples, further demonstrating that the luminescence properties are attributed to the  $Tb^{3+}$  and not to other chemical agents.

Figs. S3 and S4 show the luminescence lifetime ( $\tau$ ) of G and GO-derived materials, respectively. The decay profile for each sample was analyzed as a single exponential component ( $RLI = A \cdot e^{-t/\tau} + C$ ). A comparison of the luminescence lifetime (see Fig. 6C) shows that neither G- nor GO- derived nanocomposites nor the incorporation of Arg, Aln, Asp and Cit significantly impact the luminescence lifetime. This indicates that the luminescence lifetime is primarily determined by the  $Tb^{3+}$  present in their structures.

Regarding the luminescence properties observed with the naked eyes (see Fig. S5) and by fluorescence confocal microscopy (see Figs. S6, S7 and S8), Ap exhibit faint fluorescence emission under UV light, typically emitting a blue or violet fluorescence. This emission was captured at 412 nm and in the red channel at 559 (Fig. S6a). According to the intensity profile, there is a high correlation between the emission corresponding to apatite as the only compound of these nanoparticles (Fig. S6b).

Fig. S7 confirms that G does not exhibit intrinsic fluorescence; however, G/nAp particles doped with  $Tb^{3+}$  showed significant fluorescence emission (Fig. S7a). The source of the fluorescence emitted in the blue spectrum was complementary and different to that emitted in the red spectrum. According to the intensity profile from the images, there is a low correlation between the emission corresponding to Ap from the blue channel and that of the red channel with a Pearson's correlation coefficient (R value) = 0.1217. This indicates that the specific fluorescence properties of Ap varied depending on the chemical composition of the particles (Fig. S7b).

Regarding the GO/nAp nanocomposites, these exhibited greater surface interaction with the Ap particles, as confirmed by the intensity profile obtained along the line shown in the images. A strong correlation was observed between the two evaluated channels. The fluorescence images captured in the blue spectrum largely overlapped with those in the red spectrum, corresponding to the fluorescence of the Ap coating of GO-Arg particles in the absence of Tb (Fig. S8 a, b).

In summary, it can be concluded that biomolecules-functionalized

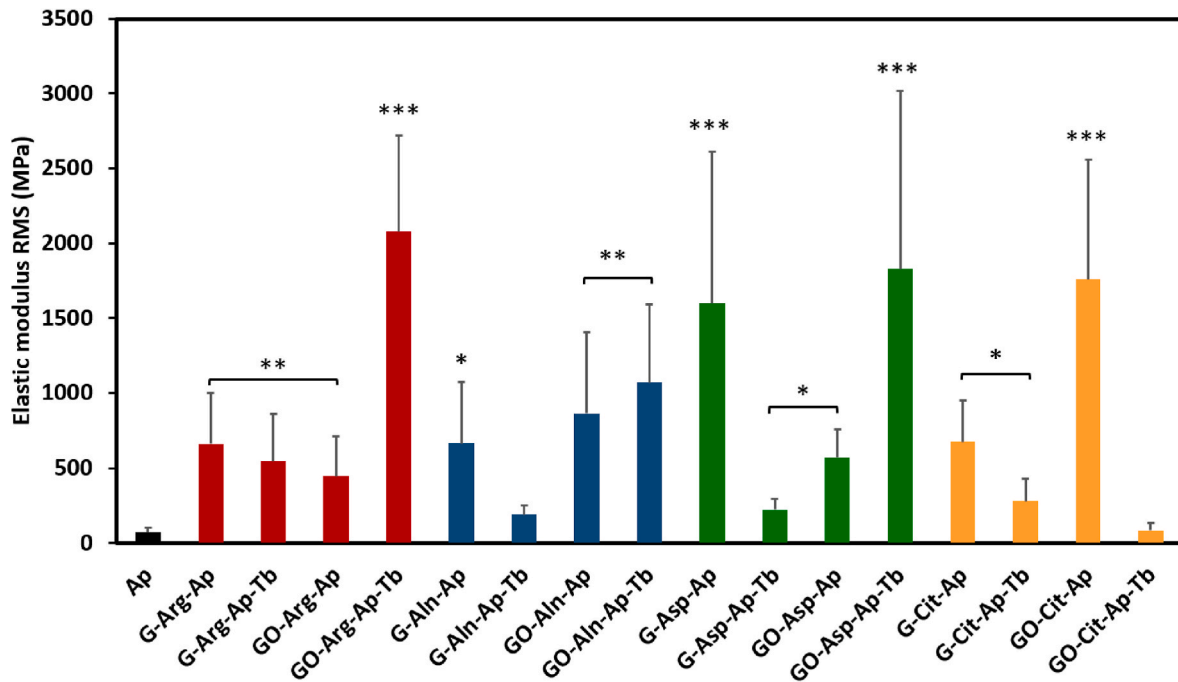


**Fig. 5.** Root Mean Square values of the elastic modulus of the G/Ap and GO/Ap nanocomposites. Data obtained by applying a 10 nN compressive load to generate force-distance curves using the Hertz model to obtain a quantitative measurement of the elastic modulus of the surface. In each sample, deformation was evaluated at 100 points per sample. G/nAp and GO/nAp, stabilized with amino acids: Arg, Aln, Asp and Cit and doped with  $Tb^{3+}$ . Statistically significant differences are presented between Ap and G/nAp and GO/nAp nanocomposites as follows: (\*)  $p < 0.05$ ; (\*\*)  $p < 0.01$ ; (\*\*\*)  $p < 0.005$ .

**Table 3**

Characterization of elastic modulus at the nanoscale by atomic force microscopy.

Particle Type	Elastic modulus $\bar{X} \pm SD^a$ (MPa)	Particle Type	Elastic modulus $\bar{X} \pm SD^a$ (MPa)
Ap	$30.2 \pm 6.5$	Ap	$30.2 \pm 6.5$
G-Arg-Ap	$138.9 \pm 65.04$	GO-Arg-Ap	$273.8 \pm 35.4$
G-Arg-Ap-Tb	$415.5 \pm 35.8$	GO-Arg-Ap-Tb	$494.9 \pm 96.5$
G-Aln-Ap	$479.9 \pm 46.2$	GO-Aln-Ap	$465.3 \pm 73.3$
G-Aln-Ap-Tb	$17.2 \pm 8.4$	GO-Aln-Ap-Tb	$3489 \pm 101.01$
G-Asp-Ap	$433.4 \pm 160$	GO-Asp-Ap	$48.1 \pm 5.74$
G-Asp-Ap-Tb	$204.4 \pm 94.7$	GO-Asp-Ap-Tb	$903.7 \pm 160$
G-Cit-Ap	$588.4 \pm 33.2$	GO-Cit-Ap	$298.1 \pm 17.46$
G-Cit-Ap-Tb	$135.3 \pm 24.5$	GO-Cit-Ap-Tb	$51.2 \pm 6.8$

<sup>a</sup>  $\bar{X} \pm SD$ : Average and Standard Deviation.

G/Ap and GO/Ap nanocomposites can be successfully doped with  $Tb^{3+}$ , to introduce luminescent properties, expanding their range of applications. These nanocomposites exhibit luminescence visible to the naked eye and are easily detectable and assessable using fluorescence microscopy, enhancing their practical utility.

### 3.4. Biological properties

The biocompatibility of Tb-doped G/Ap and GO/Ap nanocomposites was evaluated using a MTT assay on the m17.ASC murine mesenchymal stem cells after 3-days incubation at different concentrations ranging from 0.1 to 100  $\mu g/mL$  as shown in Fig. 7.

As expected, no significant toxicity was observed in the mesenchymal stem cells when treated with Ap at any concentration (Fig. 7 A, B, C, D), with the cell viability higher than 80 % in all conditions tested.

G and GO flakes exhibited a similar pattern to Ap, but only at the lowest concentration of 0.1  $\mu g/mL$ . When G/Ap nanocomposites were obtained after treatment of the flakes with the different biomolecules, G-Asp-Ap and G-Cit-Ap showed the best biocompatibility compared to the G flakes even at the highest concentration tested (Fig. 7A). However, when G-Ap were doped with  $Tb^{3+}$  (Fig. 7B), the biocompatibility was significantly decreased to around 60 %. Conversely, G-Cit-Ap-Tb was the only sample able to maintain biocompatibility above 80 % at the lowest dose of 0.1  $\mu g/mL$ .

GO/Ap nanocomposites affected cell biocompatibility: regardless the presence or absence of  $Tb^{3+}$  (Fig. 7C and D, respectively), cell viability decreased starting at 1  $\mu g/mL$  and continued to decline in a dose dependent manner up to the highest concentration tested. Indeed, 0.1  $\mu g/mL$  proved to be the most favorable concentration tested, as GO-Aln-Ap, GO-Arg-Ap, GO-Asp-Ap and GO-Cit-Ap maintained the same biocompatibility characteristics as nAp, improving the viability compared to naïve GO flakes. This effect can be due to the fact that GO induce the formation of reactive oxygen species (ROS), causing cellular oxidative stress [76].

As expected, soluble DOXO, used as internal control, exerts its activity of intercalating agent blocking cell proliferation.

## 4. Discussion

Apatite has been extensively used as a bioactive material in clinical practice to repair small bone and periodontal defects, among other applications. Nevertheless, the limited tensile strength, fracture toughness, and wear resistance of Ap have constrained its use in other areas [77]. These limitations prompted us to develop Ap-nanocomposites reinforced with G and GO nanoflakes. Arg, Aln, Asp and Cit were introduced during the exfoliation of G by LPE as well as to functionalize GO flakes, adding functional groups and binding sites for CaP nucleation. To induce the precipitation of bone-like apatite, G and GO flakes underwent mineralization by the VDSD method [35,37].

Studies of  $\zeta$ -potential and particle size distribution revealed a significant degree of aggregation, with the  $\zeta$ -potential approaching zero



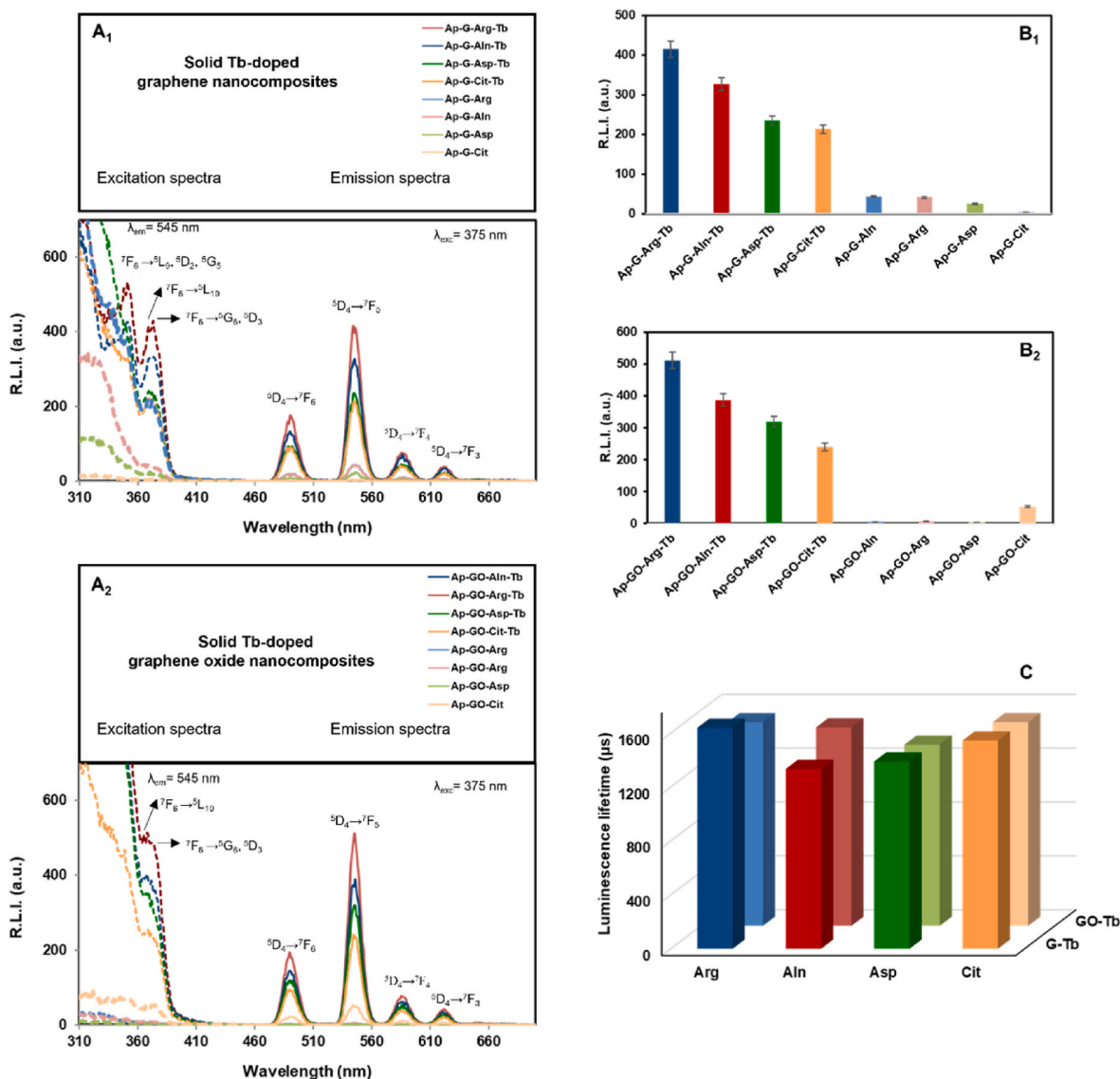


**Fig. 6.** A) Uncorrected excitation (dashed lines) and emission (solid lines) spectra of different Tb-doped A<sub>1</sub>) G-nAp and A<sub>2</sub>) GO-nAp nanocomposites. B) Relative luminescence intensity of the different Tb-doped B<sub>1</sub>) G-nAp and B<sub>2</sub>) GO-nAp nanocomposites.  $\lambda_{exc/em} = 375/545$  nm, slit-width<sub>exc/em</sub> = 10/10 nm,  $t_d = 120$  μs,  $t_g = 5$  ms and voltage detector = 700v. C) Luminescence lifetime comparison between the different Tb<sup>3+</sup>-doped nanocomposites.  $\lambda_{exc/em} = 375/545$  nm, slit-width<sub>exc/em</sub> = 20/20 nm, and detector voltage = 800 V.

after mineralization in all composites. This resulted in substantial increases in composite dimensions. FESEM and TEM analyses confirm that G and GO flakes were mineralized with needle-like apatite nanocrystals (see Fig. 4 and S2). The samples exhibited a polydisperse population of G and GO flakes with irregular shapes and sizes ranging from 50 to 200 in width and length. G flakes were discernible at very low voltages (1–3 kV) in FESEM, but became transparent at higher voltages due to their thinness. TEM images further revealed the flakes are multi-layered. As expected, the heterogeneous nucleation of apatite on the G and GO flakes occurred, with no apatite observed outside the flakes. Amino acids likely contributed as nucleation sites, suggesting they were adsorbed onto the flakes. In this context, visible spectroscopic signals of the amino acids were detected in the FTIR spectra of the nanocomposites within the wavenumber range from 1300 cm<sup>-1</sup> to 1700 cm<sup>-1</sup>, indicating the presence of –COO<sup>-</sup> and –NH<sub>3</sub><sup>+</sup> functional groups. These signals showed higher relative intensity compared to –PO<sub>4</sub> bands in the Tb-doped GO/Ap composites, while in the other composites exhibited much lower relative intensity.

In GO flakes, the hydrophilicity of the surface is attributed to the

presence of oxygen-containing functional groups such as epoxides (C–O–C), hydroxyl (–OH), carboxylic acids (–COOH), and other carbonyls (C=O) groups [78]. Based on the i.e.p. of the amino acids, and the pK<sub>a</sub> of Cit, their interaction with the oxygenated surface groups of the GO at the pH of the GO suspension (1.73), likely occurs through their –NH<sub>2</sub> groups, for instance via amides formation (–C=ON–R<sub>1</sub>R<sub>2</sub>, –C=ONH–R), or, in the case of Cit, through –COOH via H-bonding. Under these conditions, biomolecules exposed –COOH/–COO<sup>-</sup> groups toward the solution, enabling them to anchor Ca<sup>2+</sup> (and Tb<sup>3+</sup>) ions necessary for mineral phase nucleation as the pH increases.

In G/nAp nanocomposites, in contrast, the FTIR signals of the amino acids are much weaker in intensity compared to the PO<sub>4</sub> bands. However, the pHs variations after LPE, from 5.23 to 7.34 with Arg, to 6.24 with Aln, to 3.85 with Asp, and to 3.30 with Cit, offer insights into the interaction of these biomolecules with the more hydrophobic surface of G. For Arg, the –NH<sub>2</sub>–H<sup>+</sup> group likely interacts with the G surface, while for Asp and Cit, it is the –COOH groups that may be involved. In the case of Aln, due to its zwitterionic nature ([CH<sub>3</sub>CH(NH<sub>3</sub><sup>+</sup>)COO<sup>-</sup>]; i.e.p. = 6.0) the amino acid likely had a near-neutral net charge (z<sup>+</sup> + z<sup>-</sup> ≈ 0) in the

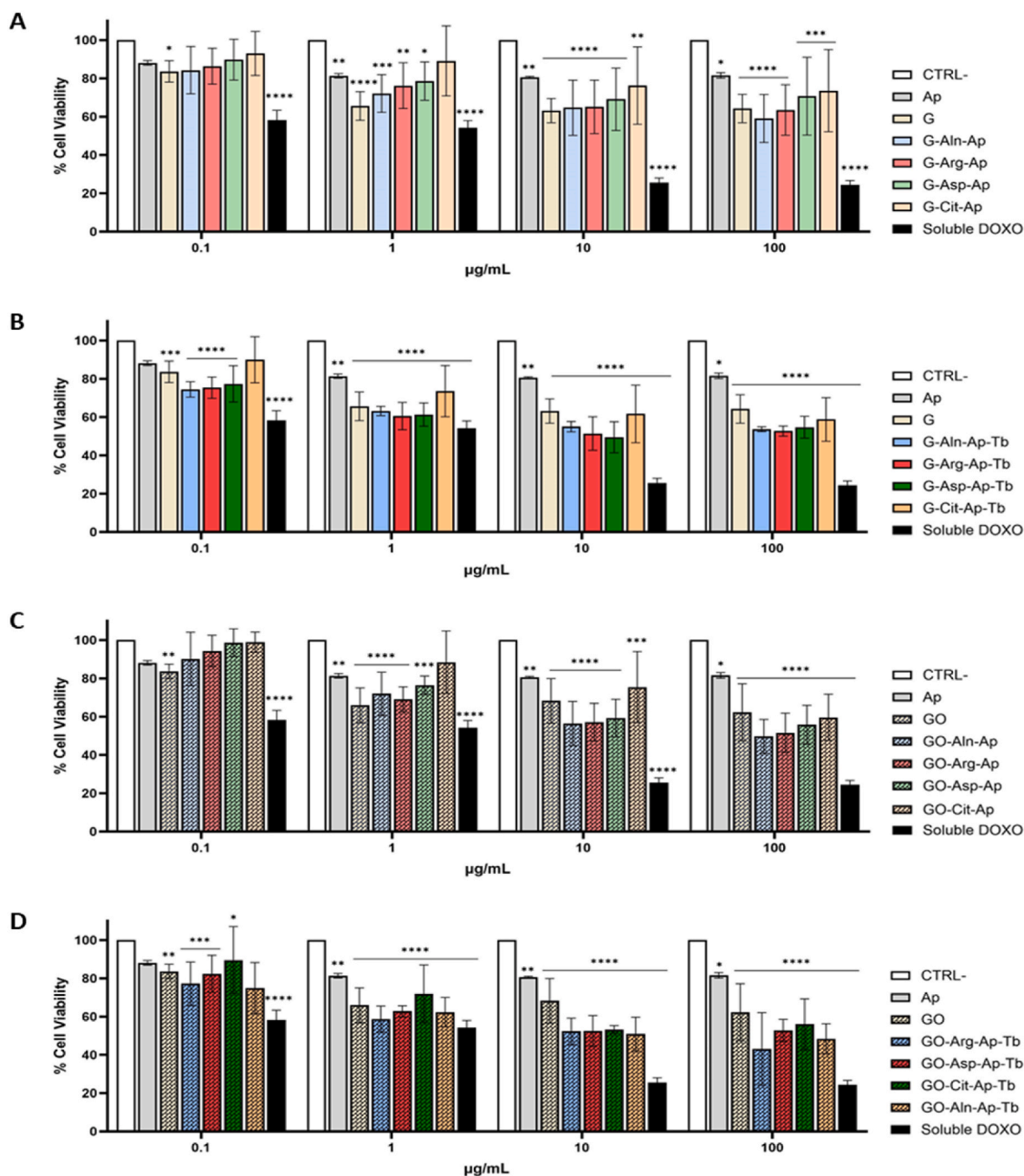


**Fig. 7.** Cytocompatibility of the different nanocomplexes Ap-based. m17.ASC cells were incubated with the several types of NPs functionalized with graphene (A) as well as Tb-doped graphene particles (B). Graphene-oxide functionalized particles were incubated within the cells (C) like Tb-doped graphene-oxide particles (D). Cells were treated for 72 h, and their viability was assessed by MTT assays. Data represent means  $\pm$  SD of three independent experiments performed in triplicates and statistical analyses were carried on using One-way ANOVA, with Dunnett comparison test. For statistical analysis all data were compared to untreated samples (CTRL-), soluble DOXO was used as internal control (\* $p < 0.05$ , \*\* $p < 0.01$ , \*\*\* $p < 0.001$ , \*\*\*\* $p < 0.0001$ ).

pH range of the exfoliation, between 5.23 and 6.24. As a nonpolar amino acid, its interaction with G could have occurred via van der Waals forces, a type of interaction also observed in the adsorption of L/D-Aln on carbon nanotubes [79].

In a set of experiments,  $\text{Tb}^{3+}$  ions were incorporated to enhance the analytical characteristics of the composites by imparting luminescence. EDX analysis clearly confirmed the presence of  $\text{Tb}^{3+}$  ions, which were observed accumulating in deposits on the flakes. Additionally, Tb signals were also uniformly distributed across the apatite surface, suggesting successful doping through  $\text{Tb}^{3+}$  to  $\text{Ca}^{2+}$  substitutions. The amount of Tb

detected via EDX showed a positive correlation with the i.e.p. of the amino acids. Notably, composites functionalized with Arginine, which has the highest i.e.p., showed the highest Tb content in the elemental analysis. This finding is consistent with luminescence spectroscopy results, where Tb-doped composites displayed excellent luminescent properties. The R.L.I. decreased in correlation with i.e.p., in the order of  $\text{Arg} > \text{Aln} > \text{Asp}$  and  $\text{pK}_1$  of Cit, which aligns with a decrease in Tb-content. This suggest that the number of deprotonated  $-\text{COO}^-$  groups available to anchor  $\text{Tb}^{3+}$  ions decreases in the same order. Furthermore, the incorporation of  $\text{Tb}^{3+}$  enables luminescence detection either by the

naked eye or by using fluorescence microscopes in the red channel. Combined with lifetime measurements (sensitized fluorescence), this imparts the materials with a broad range of potential applications in imaging and diagnostics.

The mechanical properties of the composites were analyzed, and results showed that G/nAp composites stabilized with Asp exhibited adhesion forces similar to those of Ap. The highest adhesion values were obtained for GO/nAp stabilized with Asp and Cit, and in those stabilized with each amino acid and Tb. SEM and AFM tests demonstrated that the nAp particles uniformly decorated the GO sheets, which in turn increased the surface roughness. Additionally, GO/Ap particles exhibited a strong tendency to form clusters due to their high adhesion force. These findings align with previous studies using GO as a nanoscale reinforcing filler in Ap coatings on pure titanium (Ti) substrate, which have shown high potential in orthopaedics and osseointegration for dental implants. Li et al. [80] also reported that the addition of GO was able to double the adhesion force of Ap coatings compared to pure Ap coatings, which is consistent with our findings for the GO nanocomposites stabilized with Asp, Cit, and Tb. This can be explained by the fact that GO contains oxygen containing functional groups, exhibits higher surface roughness, and stronger adhesion forces than graphene, allowing for better dispersion and interaction with nanoparticles like apatite. Furthermore, evidence has shown that incorporating GO to Ap coatings reduces surface crack propagation, enhances the bond strength of the coating to titanium (Ti), and increases corrosion resistance, all of which promote biocompatibility [81]. Moreover, the addition of GO creates a bioactive surface with antimicrobial properties [82], further enhancing its potential in biomedical applications.

The elastic modulus data exhibited significant variations with extreme values of the G or GO/nAp composites, depending on the indented area on the composite surface. The use of a blunt probe AFM instrument maps variations in nanoscale mechanical properties with good spatial resolution with the use of a small size (30  $\mu\text{m}$ ) indentation probe. This improved spatial resolution allows modulus measurements to be recorded from single particles and therefore opens the potential for spatial mapping of elastic modulus to identify local heterogeneities between crystalline domains and amorphous domains [83]. The elastic modulus values are presented in both RMS (Fig. 5) and averages (Table 3) with standard deviations because RMS is less sensitive to outliers and offers a more robust representation for heterogeneous materials like these composites. RMS captures data fluctuations more comprehensively, while averages and standard deviations help visualize symmetry and dispersion. RMS also highlights significant variation across the sample, particularly in two-phase compositions, which may cause broad error bars depending on the indentation area.

Although the probe-sample interaction is complex, the Hertzian model generates force-indentation curves that indicate that Hertzian conditions of elastic deformation are achieved without exceeding the elastic limit of the sample. However, the model does not account for the interpenetration between surfaces during the process of indentation or deformation of the AFM tip [84]. The functionalized GO/Ap nanocomposites exhibited greater surface roughness compared to G/Ap particles, regardless of the amino acid used for functionalization of the flakes. The presence of  $\text{Tb}^{3+}$  further increased surface roughness in both G/Ap and GO/Ap particles. The adhesion force of Ap was higher than that of G/Ap and GO/Ap nanocomposites stabilized with Arg and Aln, with or without  $\text{Tb}^{3+}$ . G/Ap particles stabilized with Asp displayed adhesion forces similar to Ap, while the highest adhesion values were observed in GO/Ap particles stabilized with Asp and Cit, as well as with both amino acids and  $\text{Tb}^{3+}$ . This approach has been shown to be effective for a range of soft to medium stiffness materials, as demonstrated in this study [85].

Regarding the findings of the mechanical properties of the nanocomposites, the incorporation of G and GO increased the elastic modulus of the Ap in all samples, ranging from 14 MPa for the GO-Cit-Ap-Tb particles to over 2 GPa for the GO-Arg-Ap-Tb nanocomposite. This

result confirms that nanocomposites reinforced with G and its oxygenated derivatives facilitate stress transfer within the composites. As a result, they can be effectively used as nanoscale reinforcing fillers of biocomposites for applications in both surface engineering and micro/nanofabrication [81].

One likely explanation for the improved mechanical performance of the nAp compounds is the fine grain strengthening mechanism. The functionalization of G and GO serves as a nucleation site for nAp crystallization, effectively restricting the growth of Ap nanoparticles. This grain refinement enhances microcrack toughening, crack branching, crack bridging, and crack deflection, thereby improving the overall durability and mechanical resilience of the composite by preventing crack propagation. GO also plays a crucial role in improving interfacial bonding with Ap, which enables more efficient stress distribution throughout the composite. This increase in load transfer efficiency, particularly from the GO, significantly contributes to the enhanced stiffness and strength of the composites [86].

Moreover, the large surface area and the presence of functional groups on GO (e.g., hydroxyl, carbonyl, and epoxide) enhance interfacial bonding with Ap, promoting better dispersion and interaction between nanoparticles. As the coverage of functional groups increases, the elastic modulus decreases due to disruptions in the  $\text{sp}^2$  carbon network, which weakens the material's mechanical strength [87]. This explains why nanocomposites with lower functional group coverage, such as those containing citric acid (GO-Cit-Ap-Tb), exhibited lower elastic modulus values.

Previous studies have proposed various molecules for functionalization, yielding a high range of outcomes. In the search for an optimal bone replacement biomaterial, CaP has been functionalized with gelatin [88], Ap-reinforced gelatin foams have been cross-linked with carbodiimide and saturated with tetracycline [89], alginates have been used to functionalize CaP, to produce Ap/alginate hydrogel formulations [90]. Additionally, Ap powders have been functionalized with chitosan [91] and chitin [92] to promote uniform particle dispersion. While several of these compounds improved cell adhesion, proliferation, or particle dissemination, the mechanical properties of the resulting compounds were often poor. This weakness has been attributed to the insertion of the Ap particles between the polymer chains, which reduces overall strength by weakening nanocomposite bonds [89]. Therefore, our findings demonstrated that G/GO-based nAp composite formation enhance resistance to elastic deformation, potentially contributing to the final strength of any material reinforced with the aforementioned composites. This reinforcement effect has been previously documented by Prakash et al. [93] through the fabrication of a nanocomposite chitosan film containing GO/Ap/gold for bone tissue engineering, achieving enhanced tensile and compressive strength in the nanocomposite films. The improvement was attributed to the nanoparticles acting as reinforcing material.

The study conducted by Suk et al. [78] provides valuable insights into the mechanical deformation of GO membranes, highlighting an effective Young's modulus of approximately  $207.6 \pm 23.4$  GPa for GO monolayers, roughly half that of graphene monolayers. In contrast, our study focused on measuring the elastic modulus of individual particles, revealing values of up to 3 GPa per particle in the G/nAp and GO/nAp nanocomposites. These nanocomposites stabilized with amino acids and doped with  $\text{Tb}^{3+}$ , exhibited a significant increase in elastic modulus values compared to nAp. However, to further enhance these values, particularly for applications in material coatings to improve osteoconduction, it may be beneficial to produce single or even overlapped multilayered structures, which could further enhance their mechanical properties. The incorporation of GO effectively enhances the adhesive properties of the HA coatings. The bonding strength between the GO/HA coating and Ti substrate doubled compared to the pure HA coating. Specifically, the adhesion force of the 5 wt% GO/HA coating increased from  $1.55 \pm 0.39$  MPa to  $3.3 \pm 0.25$  MPa [26], illustrating the potential for GO to significantly improve coating performance.

Specifically, in dentistry, it has been reported that the addition of G can improve the mechanical, tribological and antibacterial properties of calcium silicate [94] and glass ionomer cement [95], aiding in the protection of the pulp-dentinal complex. These compounds not only increase Vickers microhardness and compressive strength but also decrease the coefficient of friction. Our findings suggest that G/GO-based Ap biocomposites could open new avenues for use in bone repair, bone augmentation, bioactive dental cements, and reinforcement of polymeric materials in dentistry. Additionally, these composites may serve as coatings for biomedical implants, expanding their potential applications in biomedical fields.

Regarding the biological properties of the nanocomposites, the optimal concentration in terms of cellular biocompatibility, after 72 h of treatment, was found to be 0.1  $\mu\text{g/mL}$ , regardless of whether G or GO nanocomposites were used. These findings align with the well-established biocompatibility of nanocomposites derived from apatite (Ap) and graphene-based compounds. Moreover, to better understand G or GO interaction with biological systems and successfully implement their application in biomedicine, it is essential to investigate their mechanisms of uptake into mammalian cells [76].

Furthermore, the exploration of these G-based Ap composites for application in regenerative medicine, particularly concerning bone tissue, has been the focus of numerous scientific studies. Various cell types including osteoblast-related cells, fibroblast-related cells and mesenchymal stem cells have been used to screen the biocompatibility of these nanocomposites, consistently demonstrating their biological potential and generating a common consensus on their value [28,96]. However, amidst the acclaim, elevated levels of GO within the composites might exert negative impact on cell viability. As a matter of fact, it has been reported that excessive GO concentrations within the composites might cause negative outcomes on cell survival [81]. Additionally, it has been reported that G and GO also enhanced the proliferation and osteogenic differentiation of stem cells comparable to common growth factors, providing a new idea for studies on the effect of G-based Ap composites for solving the clinical problem of bone defects [97].

Furthermore, the introduction of terbium (Tb) ions into the nanocomposites adds yet another important variable to be considered into the biocompatibility evaluation. Despite the widespread utilization of Tb within the biomedical area due to its favorable physicochemical properties and its natural affinity for deposition within bone tissue, the concentrations used in the preparation of the nanocomposites outlined herein warrant examination [98]. The reduced biocompatibility observed in Tb-doped G/Ap nanocomposites, particularly around 60 %, may be attributed to the cytotoxic effects of terbium ions, which can disrupt cellular functions at higher concentrations. While terbium offers useful luminescent properties for bioimaging, its interaction with cells can lead to cytotoxicity at high  $\text{Tb}^{3+}$  concentrations. However, when functionalized with citric acid (G-Cit-Ap-Tb), the biocompatibility remained high, likely due to citric acid's stabilizing effect, which may reduce the harmful impact of  $\text{Tb}^{3+}$  ions by minimizing their direct interaction with cellular components [99]. A reduction in Tb concentration may be advisable to alleviate undue cellular stress, particularly on sensitive cell types, such as m17.ASC.

Similarly, the dose-dependent reduction in biocompatibility of GO-Ap nanocomposites, especially at concentrations above 1  $\mu\text{g/mL}$ , aligns with the known effects of GO in generating reactive oxygen species (ROS), leading to oxidative stress. GO's ability to produce ROS can result in oxidative damage to cellular components such as lipids, proteins and DNA, ultimately causing cell membrane disruption and apoptosis. The sharp edges and large surface area of GO exacerbate this issue by facilitating interactions with the cell membrane [100]. However, functionalizing GO with biomolecules like arginine, aspartic acid, and citric acid has been shown to mitigate these effects. This modification reduces oxidative stress by stabilizing the GO flakes and decreasing their direct interactions with cells, thus improving biocompatibility at lower concentrations. Furthermore, functionalization

enhances the ability of nanocomposites to disperse and interact more effectively with the biological environment, minimizing cytotoxicity and promoting better stress distribution across the composite [101].

## 5. Conclusions

In conclusion, this study demonstrates the successful synthesis of hybrid nanocomposites through the heterogeneous nucleation of calcium phosphate (apatite) on functionalized G and GO flakes using the SDVD. This approach enabled the precise deposition of nAp on the flakes, resulting in composites with enhanced mechanical and functional properties. The addition of amino acids and  $\text{Tb}^{3+}$  ions significantly improved surface roughness, adhesion, and elastic modulus, making these materials highly suitable for a variety of applications in hard tissue engineering and dental regeneration. In addition, the nanocomposites doped with  $\text{Tb}^{3+}$  exhibit luminescent properties making them visible to the naked eye and easily detectable/evaluable via fluorescence microscopy. The R.L.I. correlates with the Tb content, which in turn increases in the order of  $\text{Arg} > \text{Aln} > \text{Asp} > \text{Cit}$ . No significant differences were observed in the R.L.I. between G and GO samples. Regarding the luminescence lifetime, it is solely dependent on the  $\text{Tb}^{3+}$  present in their structures, and neither the G- nor GO- derived nanocomposites nor the incorporation of Arg, Aln, Asp and Cit significantly affected the luminescence lifetime.

Lastly, the Ap/G and Ap/GO nanocomposites demonstrated biocompatibility, with cell viability exceeding 80 % at lower concentrations (0.1  $\mu\text{g/mL}$ ) in mesenchymal stem cells. However, higher concentrations of  $\text{Tb}^{3+}$  led to a decrease in viability compared to undoped composites. These findings highlight the need for careful regulation of both nanocomposite dosage and  $\text{Tb}^{3+}$  concentration to ensure optimal cell compatibility while retaining the desired properties for biomedical applications. Future research should focus on optimizing the formulation to ensure consistency, enhance biocompatibility, and minimize cytotoxic effects. Additionally, further *in vivo* studies are necessary to validate the long-term performance and safety of these nanocomposites, particularly in bone and dental tissue regeneration.

Overall, the findings underscore the potential of G/GO-based apatite nanocomposites as multifunctional materials, offering improved mechanical properties and added functionalities, making them promising candidates for biomedical applications, particularly in tissue regeneration and implant coatings.

## CRedit authorship contribution statement

**Francisco Javier Acebedo-Martínez:** Writing – review & editing, Writing – original draft, Methodology, Investigation. **Paula Alejandra Baldiño:** Writing – original draft, Methodology, Investigation, Conceptualization. **Francesca Oltolina:** Writing – original draft, Methodology, Investigation. **Antonia Follenzi:** Supervision, Methodology, Investigation. **Giuseppe Falini:** Writing – review & editing, Methodology, Conceptualization. **Jorge Fernando Fernández-Sánchez:** Writing – original draft, Methodology, Investigation. **Duane Choquesillo-Lazarte:** Investigation, Funding acquisition. **Jaime Gómez-Morales:** Writing – review & editing, Writing – original draft, Supervision, Project administration, Methodology, Data curation, Conceptualization.

## Declaration of competing interest

The authors declare that they have no known competing financial interests or personal relationships that could have appeared to influence the work reported in this paper.

## Acknowledgements

Spanish Agencia Estatal de Investigación of the Ministerio de Ciencia



e Innovación y Universidades (MCIU), Bioscaffold project, ref. PGC2018-102047-B-I00 (MCIU/AEI/FEDER, UE), funded this research. FJAM acknowledge FPIgrant (Ref. PRE2019-088832) funded by the Spanish Agencia Estatal de Investigación of the MCIU. The authors acknowledge technical support from Raquel Fernández Penas and technicians of SEM and TEM of the CIC of the University of Granada. All authors contributed equally to this work.

## Appendix A. Supplementary data

Supplementary data to this article can be found online at <https://doi.org/10.1016/j.ceramint.2024.10.034>.

## References

- [1] S. Pina, J.M. Oliveira, R.L. Reis, Natural-based nanocomposites for bone tissue engineering and regenerative medicine: a review, *Adv. Mater.* 27 (2015) 1143–1169, <https://doi.org/10.1002/adma.201403354>.
- [2] Y.Y. Hu, A. Rawal, K. Schmidt-Rohr, Strongly bound citrate stabilizes the apatite nanocrystals in bone, *Proc. Natl. Acad. Sci. U. S. A.* 107 (2010) 22425–22429, <https://doi.org/10.1073/PNAS.1009219107/ASSET/B53276B2-073E-40A7-B8F7-E28AC70040CD/ASSETS/GRAPHIC/PNAS.1009219107EQ8.GIF>.
- [3] J.M. Delgado-López, R. Frison, A. Cervellino, J. Gómez-Morales, A. Guagliardi, N. Masciocchi, Crystal size, morphology, and growth mechanism in bio-inspired apatite nanocrystals, *Adv. Funct. Mater.* 24 (2014) 1090–1099, <https://doi.org/10.1002/ADFM.201302075>.
- [4] M. Iafisco, G.B. Ramírez-Rodríguez, Y. Sakhno, A. Tampieri, G. Martra, J. Gómez-Morales, J.M. Delgado-López, The growth mechanism of apatite nanocrystals assisted by citrate: relevance to bone biomineralization, *CrystEngComm* 17 (2014) 507–511, <https://doi.org/10.1039/C4CE01415D>.
- [5] P. Ivanchenko, J.M. Delgado-López, M. Iafisco, J. Gómez-Morales, A. Tampieri, G. Martra, Y. Sakhno, On the surface effects of citrates on nano-apatites: evidence of a decreased hydrophilicity, *Sci. Rep.* 7 (2017) 1–10, <https://doi.org/10.1038/s41598-017-09376-x>, 2017.
- [6] K. Sato, Y. Kumagai, J. Tanaka, Apatite formation on organic monolayers in simulated body environment, [https://doi.org/10.1002/\(SICI\)1097-4636\(200004\)50:1, 2000](https://doi.org/10.1002/(SICI)1097-4636(200004)50:1, 2000).
- [7] M.A. Martins, C. Santos, M.M. Almeida, M.E.V. Costa, Hydroxyapatite micro- and nanoparticles: nucleation and growth mechanisms in the presence of citrate species, *J. Colloid Interface Sci.* 318 (2008) 210–216, <https://doi.org/10.1016/J.JCIS.2007.10.008>.
- [8] D.R. Talham, Biomineralization: principles and concepts in bioinorganic materials chemistry stephen mann, in: *Cryst. Growth Des.*, vol. 2, Oxford University Press, New York, 2002, p. 675, <https://doi.org/10.1021/cg020033l>, 675, 2001.
- [9] J. Gómez-Morales, M. Iafisco, J.M. Delgado-López, S. Sarda, C. Drouet, Progress on the preparation of nanocrystalline apatites and surface characterization: overview of fundamental and applied aspects, *Prog. Cryst. Growth Char. Mater.* 59 (2013) 1–46, <https://doi.org/10.1016/J.PCRYSGROW.2012.11.001>.
- [10] S. Cazalbou, D. Eichert, X. Ranz, C. Drouet, C. Combes, M.F. Harmand, C. Rey, Ion exchanges in apatites for biomedical application, *J. Mater. Sci. Mater. Med.* 16 (2005) 405–409, <https://doi.org/10.1007/S10856-005-6979-2/METRICS>.
- [11] S.C. Cox, J.A. Thornby, G.J. Gibbons, M.A. Williams, K.K. Mallick, 3D printing of porous hydroxyapatite scaffolds intended for use in bone tissue engineering applications, *Mater. Sci. Eng. C* 47 (2015) 237–247, <https://doi.org/10.1016/j.msec.2014.11.024>.
- [12] K. Zhang, K. Zeng, C. Shen, S. Tian, M. Yang, Determination of protein kinase A activity and inhibition by using hydroxyapatite nanoparticles as a fluorescent probe, *Microchim. Acta* 185 (2018) 1–7, <https://doi.org/10.1007/s00604-018-2754-1>.
- [13] V. Mourinho, A.R. Boccaccini, Bone tissue engineering therapeutics: controlled drug delivery in three-dimensional scaffolds, *J. R. Soc. Interface* 7 (2010) 209–227, <https://doi.org/10.1098/rsif.2009.0379>.
- [14] C.P. Charalambous, Calcium phosphate ceramics as hard tissue prosthetics, in: *Class. Pap. Orthop.*, Springer-Verlag London Ltd, 2014, pp. 419–421, [https://doi.org/10.1007/978-1-4471-5451-8\\_106](https://doi.org/10.1007/978-1-4471-5451-8_106).
- [15] M. Vallet-Regí, J.M. González-Calbet, Calcium phosphates as substitution of bone tissues, *Prog. Solid State Chem.* 32 (2004) 1–31, <https://doi.org/10.1016/j.prosolidchem.2004.07.001>.
- [16] S. Bose, M. Roy, A. Bandyopadhyay, Recent advances in bone tissue engineering scaffolds, *Trends Biotechnol.* 30 (2012) 546–554, <https://doi.org/10.1016/j.tibtech.2012.07.005>.
- [17] L. Fathyunes, J. Khalil-Allafi, S.O.R. Sheykholsami, M. Moosavifar, Biocompatibility assessment of graphene oxide-hydroxyapatite coating applied on TiO<sub>2</sub> nanotubes by ultrasound-assisted pulse electrodeposition, *Mater. Sci. Eng. C* 87 (2018) 10–21, <https://doi.org/10.1016/j.msec.2018.02.012>.
- [18] E.F. Morgan, D.N. Yetkinler, B.R. Constantz, R.H. Dauskardt, Mechanical properties of carbonated apatite bone mineral substitute: strength, fracture and fatigue behaviour, *J. Mater. Sci. Mater. Med.* 8 (1997) 559–570, <https://doi.org/10.1023/A:1018550831834/METRICS>.
- [19] S. Pina, J.M. Oliveira, R.L. Reis, Natural-based nanocomposites for bone tissue engineering and regenerative medicine: a review, *Adv. Mater.* 27 (2015) 1143–1169, <https://doi.org/10.1002/ADMA.201403354>.
- [20] R. Hsissou, R. Seghiri, Z. Benzekri, M. Hilali, M. Rafik, A. Elharfi, Polymer composite materials: a comprehensive review, *Compos. Struct.* 262 (2021) 113640, <https://doi.org/10.1016/J.COMPSTRUCT.2021.113640>.
- [21] H. Bai, C. Li, G. Shi, H. Bai, C. Li, G.Q. Shi, Functional composite materials based on chemically converted graphene, *Adv. Mater.* 23 (2011) 1089–1115, <https://doi.org/10.1002/ADMA.201003753>.
- [22] U. Farooq, A.K. Qureshi, M. Farhan, U. Romman, M.E. Khan, W. Ali, A.H. Bashiri, W. Zakri, Environmentally sustainable fabrication of palladium nanoparticles from the ethanolic crude extract of *Oxystelma esculentum* towards effective degradation of organic dye, *Today Sustain.* 23 (2023) 100463, <https://doi.org/10.1016/J.MTSUST.2023.100463>.
- [23] U. Farooq, M. Raza, S. Ali Khan, S. Alam, M. Ehtisham Khan, W. Ali, W. Al Zoubi, S. Kashif Ali, A.H. Bashiri, W. Zakri, Fabrication and characterization of binary composite MgO/CuO nanostructures for the efficient photocatalytic ability to eliminate organic contaminants: a detailed spectroscopic analysis, *Spectrochim. Acta Part A Mol. Biomol. Spectrosc.* 315 (2024) 124264, <https://doi.org/10.1016/J.SAA.2024.124264>.
- [24] M. Imran, M. Raza, H. Noor, S.M. Faraz, A. Raza, U. Farooq, M.E. Khan, S.K. Ali, O.Y. Bakather, W. Ali, A.H. Bashiri, W. Zakri, Insight into mechanism of excellent visible-light photocatalytic activity of CuO/MgO/ZnO nanocomposite for advanced solution of environmental remediation, *Chemosphere* 359 (2024) 142224, <https://doi.org/10.1016/J.CHEMOSPHERE.2024.142224>.
- [25] M. Raza, U. Farooq, S. Ali Khan, Z. Ullah, M. Ehtisham Khan, S. Kashif Ali, O. Y. Bakather, S. Alam, M. Yasir Khan, W. Ali, A. Ulla Khan, W. Al Zoubi, A. H. Bashiri, W. Zakri, Preparation and Spectrochemical characterization of Ni-doped ZnS nanocomposite for effective removal of emerging contaminants and hydrogen production: reaction kinetics, mechanistic insights, *Spectrochim. Acta Part A Mol. Biomol. Spectrosc.* 318 (2024) 124513, <https://doi.org/10.1016/J.SAA.2024.124513>.
- [26] M. Raza, U. Farooq, M.E. Khan, K. Naseem, S. Alam, M.Y. Khan, W. Ali, S.K. Ali, O.Y. Bakather, W. Al Zoubi, A.H. Bashiri, W. Zakri, Development of simplistic and stable Co-doped ZnS nanocomposite towards excellent removal of bisphenol A from wastewater and hydrogen production: evaluation of reaction parameters by response surface methodology, *J. Taiwan Inst. Chem. Eng.* 163 (2024) 105654, <https://doi.org/10.1016/J.JTICE.2024.105654>.
- [27] H. Noor, A. Zafar, A. Raza, A. Baqi, U. Farooq, M.E. Khan, W. Ali, S.K. Ali, A. H. Bashiri, W. Zakri, Advancement in optical and dielectric properties of unsaturated polyester resin/zinc oxide nanocomposite: synthesis to application in electronics, *J. Mater. Sci. Mater. Electron.* 35 (2024) 1–14, <https://doi.org/10.1007/S10854-024-13357-Y/FIGURES/11>.
- [28] M. Li, P. Xiong, F. Yan, S. Li, C. Ren, Z. Yin, A. Li, H. Li, X. Ji, Y. Zheng, Y. Cheng, An overview of graphene-based hydroxyapatite composites for orthopedic applications, *Bioact. Mater.* 3 (2018) 1–18, <https://doi.org/10.1016/J.BIOACTMAT.2018.01.001>.
- [29] E.J. Duplock, M. Scheffler, P.J.D. Lindan, Hallmark of perfect graphene, *Phys. Rev. Lett.* 92 (2004) 225502, <https://doi.org/10.1103/PHYSREVLETT.92.225502/FIGURES/4/MEDIUM>.
- [30] C. Lee, X. Wei, J.W. Kysar, J. Hone, Measurement of the elastic properties and intrinsic strength of monolayer graphene, *Science* 321 (2008) 385–388, [https://doi.org/10.1126/SCIENCE.1157996/SUPPL\\_FILE/LEE-SOM.PDF](https://doi.org/10.1126/SCIENCE.1157996/SUPPL_FILE/LEE-SOM.PDF).
- [31] K. Yang, H. Gong, X. Shi, J. Wan, Y. Zhang, Z. Liu, In vivo biodistribution and toxicology of functionalized nano-graphene oxide in mice after oral and intraperitoneal administration, *Biomaterials* 34 (2013) 2787–2795, <https://doi.org/10.1016/J.BIOMATERIALS.2013.01.001>.
- [32] S. Stankovich, D.A. Dikin, G.H.B. Dommett, K.M. Kohlhaas, E.J. Zimney, E. A. Stach, R.D. Piner, S.B.T. Nguyen, R.S. Ruoff, Graphene-based composite materials, *Nat* 442 (2006) 282–286, <https://doi.org/10.1038/nature04969>, 2006 4427100.
- [33] W. Gao, The chemistry of graphene oxide, *Graphene Oxide Reduct, Recipes, Spectrosc. Appl.* (2015) 61–95, [https://doi.org/10.1007/978-3-319-15500-5\\_3/COVER](https://doi.org/10.1007/978-3-319-15500-5_3/COVER).
- [34] A. Cai, R.E. Horch, J.P. Beier, Nanofiber composites in skeletal muscle tissue engineering, *Nanofiber Compos. Biomed. Appl.* (2017) 369–394, <https://doi.org/10.1016/B978-0-08-100173-8.00015-6>.
- [35] Y. Wu, Y. Wang, S. Tian, Y. Jing, J. Zhuang, L. Guo, D. Jia, Y. Zhou, Hydrothermal fabrication of rGO/Apatite layers on AZ31 magnesium alloy for enhanced bonding strength and corrosion resistance, *Appl. Surf. Sci.* 470 (2019) 430–438, <https://doi.org/10.1016/j.apsusc.2018.11.086>.
- [36] J.D. Núñez, A.M. Benito, R. González, J. Aragón, R. Arenal, W.K. Maser, Integration and bioactivity of hydroxyapatite grown on carbon nanotubes and graphene oxide, *Carbon N. Y.* 79 (2014) 590–604, <https://doi.org/10.1016/j.carbon.2014.08.020>.
- [37] H. Liu, P. Xi, G. Xie, Y. Shi, F. Hou, L. Huang, F. Chen, Z. Zeng, C. Shao, J. Wang, Simultaneous reduction and surface functionalization of graphene oxide for hydroxyapatite mineralization, *J. Phys. Chem. C* 116 (2012) 3334–3341, <https://doi.org/10.1021/jp2102226>.
- [38] A. Janković, S. Eraković, M. Mitrić, I.Z. Matic, Z.D. Juranić, G.C.P. Tsui, C. Y. Tang, V. Mišković-Stanković, K.Y. Rhee, S.J. Park, Bioactive hydroxyapatite/graphene composite coating and its corrosion stability in simulated body fluid, *J. Alloys Compd.* 624 (2015) 148–157, <https://doi.org/10.1016/j.jallcom.2014.11.078>.
- [39] C. Fu, H. Bai, J. Zhu, Z. Niu, Y. Wang, J. Li, X. Yang, Y. Bai, Enhanced cell proliferation and osteogenic differentiation in electrospun PLGA/hydroxyapatite

- nanofibre scaffolds incorporated with graphene oxide, *PLoS One* 12 (2017), <https://doi.org/10.1371/journal.pone.0188352>.
- [40] I. Iacoboni, F. Perrozzi, L. Macera, G. Taglieri, L. Ottaviano, G. Fioravanti, In situ syntheses of hydroxyapatite-grafted graphene oxide composites, *J. Biomed. Mater. Res., Part A* 107 (2019) 2026–2039, <https://doi.org/10.1002/jbm.a.36716>.
- [41] J. Gómez-Morales, L.A. González-Ramírez, C. Verdugo-Escamilla, R.F. Penas, F. Oltolina, M. Prat, G. Falini, Induced nucleation of biomimetic nanoapatites on exfoliated graphene biomolecule flakes by vapor diffusion in microdroplets, *Crystals* 9 (2019) 1–12, <https://doi.org/10.3390/cryst9070341>.
- [42] J. Gómez-Morales, C. Verdugo-Escamilla, J.A. Gavira, Bioinspired calcium phosphate coated mica sheets by vapor diffusion and its effects on lysozyme assembly and crystallization, *Cryst. Growth Des.* 16 (2016) 5150–5158, <https://doi.org/10.1021/acs.cgd.6b00716>.
- [43] A. Torres-Mansilla, P. Álvarez-Lloret, A. Voltes-Martínez, E. López-Ruiz, P. A. Baldián, J.A. Marchal, J. Gómez-Morales, Apatite-coated outer layer eggshell membrane: a novel osteoinductive biohybrid composite for guided bone/tissue regeneration, *Biomater. Adv.* 154 (2023) 213605, <https://doi.org/10.1016/j.bioadv.2023.213605>.
- [44] A. Ciesielski, P. Samorì, Graphene via sonication assisted liquid-phase exfoliation, *Chem. Soc. Rev.* 43 (2014) 381–398, <https://doi.org/10.1039/c3cs60217f>.
- [45] J.M. Delgado-López, M. Iafisco, I. Rodríguez, A. Tampieri, M. Prat, J. Gómez-Morales, Crystallization of bioinspired citrate-functionalized nanoapatite with tailored carbonate content, *Acta Biomater.* 8 (2012) 3491–3499, <https://doi.org/10.1016/j.actbio.2012.04.046>.
- [46] J. Gómez-Morales, J.M. Delgado-López, M. Iafisco, A. Hernández-Hernández, M. Prat, Amino acidic control of calcium phosphate precipitation by using the vapor diffusion method in microdroplets, *Cryst. Growth Des.* 11 (2011) 4802–4809, [https://doi.org/10.1021/CG2004547/ASSET/IMAGES/LARGE/CG-2011-004547\\_0008.JPEG](https://doi.org/10.1021/CG2004547/ASSET/IMAGES/LARGE/CG-2011-004547_0008.JPEG).
- [47] W. Schneiders, A. Reinstorf, W. Pompe, R. Grass, A. Biewener, M. Holch, H. Zwipp, S. Rammelt, Effect of modification of hydroxyapatite/collagen composites with sodium citrate, phosphoserine, phosphoserine/RGD-peptide and calcium carbonate on bone remodeling, *Bone* 40 (2007) 1048–1059, <https://doi.org/10.1016/j.bone.2006.11.019>.
- [48] U. Hempel, A. Reinstorf, M. Poppe, U. Fischer, M. Gelinsky, W. Pompe, K. W. Wenzel, Proliferation and differentiation of osteoblasts on Biocement D modified with collagen type I and citric acid, *J. Biomed. Mater. Res. Part B Appl. Biomater.* 71B (2004) 130–143, <https://doi.org/10.1002/jbm.b.30082>.
- [49] J. Gómez-Morales, R. Fernández-Penas, F.J. Acebedo-Martínez, I. Romero-Castillo, C. Verdugo-Escamilla, D. Choquesillo-Lazarte, L.D. Esposti, Y. Jiménez-Martínez, J.F. Fernández-Sánchez, M. Iafisco, H. Boulaiz, Luminescent citrate-functionalized terbium-substituted carbonated apatite nanomaterials: structural aspects, sensitized luminescence, cytocompatibility, and cell uptake imaging, *Nanomaterials* 12 (2022) 1257, <https://doi.org/10.3390/NANO12081257/S1>.
- [50] A. Al-Kattan, V. Santran, P. Dufour, J. Dexpert-Ghys, C. Drouet, Novel contributions on luminescent apatite-based colloids intended for medical imaging, *J. Biomater. Appl.* 28 (2014) 697–707, <https://doi.org/10.1177/0885328212473510/ASSET/IMAGES/LARGE/10.1177.0885328212473510-FIG7.JPEG>.
- [51] Y. Wang, Y. Lu, J. Zhang, X. Hu, Z. Yang, Y. Guo, Y. Wang, A synergistic antibacterial effect between terbium ions and reduced graphene oxide in a poly (vinyl alcohol)-alginate hydrogel for treating infected chronic wounds, *J. Mater. Chem. B* 7 (2019) 538–547, <https://doi.org/10.1039/C8TB02679C>.
- [52] D.D. Liu, K. Ge, Y. Jin, J. Sun, S.X. Wang, M.S. Yang, J.C. Zhang, Terbium promotes adhesion and osteogenic differentiation of mesenchymal stem cells via activation of the Smad-dependent TGF- $\beta$ /BMP signaling pathway, *J. Biol. Inorg. Chem.* 19 (2014) 879–891, <https://doi.org/10.1007/S00775-014-1119-4/FIGURES/12>.
- [53] I. Romero-Castillo, E. López-Ruiz, J.F. Fernández-Sánchez, J.A. Marchal, J. Gómez-Morales, Self-Assembled type I collagen-apatite fibers with varying mineralization extent and luminescent terbium promote osteogenic differentiation of mesenchymal stem cells, *Macromol. Biosci.* 21 (2021) 2000319, <https://doi.org/10.1002/MABI.202000319>.
- [54] L. Li, Y. Liu, J. Tao, M. Zhang, H. Pan, X. Xu, R. Tang, Surface modification of hydroxyapatite nanocrystallite by a small amount of terbium provides a biocompatible fluorescent probe, *J. Phys. Chem. C* 112 (2008) 12219–12224, [https://doi.org/10.1021/JP8026463/ASSET/IMAGES/LARGE/JP-2008-026463\\_0009.JPEG](https://doi.org/10.1021/JP8026463/ASSET/IMAGES/LARGE/JP-2008-026463_0009.JPEG).
- [55] L.J. Sun, P.F. Ni, D.G. Guo, C.Q. Fang, J. Wang, F. Yang, X.F. Huang, Y.Z. Hao, H. Zhu, K.W. Xu, Synthesis and characterization of Tb-incorporated apatite nanoscale powders, *J. Mater. Sci. Technol.* 28 (2012) 773–778, [https://doi.org/10.1016/S1005-0302\(12\)60129-7](https://doi.org/10.1016/S1005-0302(12)60129-7).
- [56] H. Maleki-Ghaleh, M.H. Siadati, A. Fallah, B. Koc, M. Kavanlouei, P. Khademi-Azandehi, E. Moradpur-Tari, Y. Omid, J. Barar, Y. Beygi-Khosrovshahi, A. P. Kumar, K. Adibkia, Antibacterial and cellular behaviors of novel zinc-doped hydroxyapatite/graphene nanocomposite for bone tissue engineering, *Int. J. Mol. Sci.* 22 (2021) 9564, <https://doi.org/10.3390/IJMS22179564> (2021) 9564.
- [57] M. Iafisco, J.G. Morales, M.A. Hernández-Hernández, J.M. García-Ruiz, N. Roveri, Biomimetic carbonate-hydroxyapatite nanocrystals prepared by vapor diffusion, *Adv. Eng. Mater.* 12 (2010) 218–223, <https://doi.org/10.1002/adem.201080003>.
- [58] N. Iwashita, X-Ray powder diffraction, *Mater. Sci. Eng. C* (2016) 7–25, <https://doi.org/10.1016/B978-0-12-805256-3.00002-7>.
- [59] L.M. Malard, M.A. Pimenta, G. Dresselhaus, M.S. Dresselhaus, Raman spectroscopy in graphene, *Phys. Rep.* 473 (2009) 51–87, <https://doi.org/10.1016/J.PHYSREP.2009.02.003>.
- [60] B. Foley, M. Greiner, G. McGlynn, W.W. Schmahl, Anatomical variation of human bone bioapatite crystallography, *Cryst* 10 (10) (2020) 859, <https://doi.org/10.3390/CRYST10100859> (2020) 859.
- [61] I. Khairoun, M.G. Boltong, F.C.M. Driessens, J.A. Planell, Effect of calcium carbonate on the compliance of an apatitic calcium phosphate bone cement, *Biomaterials* 18 (1997) 1535–1539, [https://doi.org/10.1016/S0142-9612\(97\)80005-1](https://doi.org/10.1016/S0142-9612(97)80005-1).
- [62] Y. Hao, Y. Wang, L. Wang, Z. Ni, Z. Wang, R. Wang, C.K. Koo, Z. Shen, J.T. L. Thong, Probing layer number and stacking order of few-layer graphene by Raman spectroscopy, *Small* 6 (2010) 195–200, <https://doi.org/10.1002/SMLL.200901173>.
- [63] A. Grunewald, C. Keyser, A.M. Sautereau, E. Crubézy, B. Ludes, C. Drouet, Revisiting carbonate quantification in apatite (bio)minerals: a validated FTIR methodology, *J. Archaeol. Sci.* 49 (2014) 134–141, <https://doi.org/10.1016/J.JAS.2014.05.004>.
- [64] A. Tsorlos, G.H. Nancollas, The adsorption of polyelectrolytes on hydroxyapatite crystals, *J. Colloid Interface Sci.* 209 (1999) 109–115, <https://doi.org/10.1006/JCIS.1998.5881>.
- [65] S. Koutsopoulos, E. Dalas, Hydroxyapatite crystallization in the presence of serine, tyrosine and hydroxyproline amino acids with polar side groups, *J. Cryst. Growth* 216 (2000) 443–449, [https://doi.org/10.1016/S0022-0248\(00\)00415-2](https://doi.org/10.1016/S0022-0248(00)00415-2).
- [66] R. Gonzalez-McQuire, J.Y. Chane-Ching, E. Vignaud, A. Lebugle, S. Mann, Synthesis and characterization of amino acid-functionalized hydroxyapatite nanorods, *J. Mater. Chem.* 14 (2004) 2277–2281, <https://doi.org/10.1039/B400317A>.
- [67] U.K. Sur, A. Saha, A. Datta, B. Ankamwar, F. Surti, S.D. Roy, D. Roy, Synthesis and characterization of stable aqueous dispersions of graphene, *Bull. Mater. Sci.* 39 (2016) 159–165, <https://doi.org/10.1007/S12034-015-0893-0/TABLES/1>.
- [68] T. Szabo, P. Maroni, I. Szilagy, Size-dependent aggregation of graphene oxide, *Carbon* N. Y. 160 (2020) 145–155, <https://doi.org/10.1016/J.CARBON.2020.01.022>.
- [69] K.E.D. Coan, B.K. Shoichet, Stoichiometry and physical chemistry of promiscuous aggregate-based inhibitors, *J. Am. Chem. Soc.* 130 (2008) 9606–9612, [https://doi.org/10.1021/JA802977H/ASSET/IMAGES/MEDIUM/JA-2008-02977H\\_0008.GIF](https://doi.org/10.1021/JA802977H/ASSET/IMAGES/MEDIUM/JA-2008-02977H_0008.GIF).
- [70] A.A. Lall, W. Rong, L. Mädlar, S.K. Friedlander, Nanoparticle aggregate volume determination by electrical mobility analysis: test of idealized aggregate theory using aerosol particle mass analyzer measurements, *J. Aerosol Sci.* 39 (2008) 403–417, <https://doi.org/10.1016/J.JAEROSCI.2007.12.010>.
- [71] N. Nassif, F. Martineau, O. Syzgantseva, F. Gobeaux, M. Willinger, T. Coradin, S. Cassaignon, T. Azais, M.M. Giraud-Guille, In vivo inspired conditions to synthesize biomimetic hydroxyapatite, *Chem. Mater.* 22 (2010) 3653–3663, <https://doi.org/10.1021/cm903596q>.
- [72] J. Gómez-Morales, C. Verdugo-Escamilla, R. Fernández-Penas, C.M. Parra-Milla, C. Drouet, F. Maube-Bosc, F. Oltolina, M. Prat, J.F. Fernández-Sánchez, Luminescent biomimetic citrate-coated europium-doped carbonated apatite nanoparticles for use in bioimaging: physico-chemistry and cytocompatibility, *RSC Adv.* 8 (2018) 2385–2397, <https://doi.org/10.1039/c7ra12536d>.
- [73] I. Hemmilä, S. Dakubu, V.M. Mukkala, H. Siitari, T. Lövgren, Europium as a label in time-resolved immunofluorometric assays, *Anal. Biochem.* 137 (1984) 335–343, [https://doi.org/10.1016/0003-2697\(84\)90095-2](https://doi.org/10.1016/0003-2697(84)90095-2).
- [74] S.M.C. Plá, A. D'urso, J.F. Fernández-Sánchez, D. Colangelo, D. Choquesillo-Lazarte, R. Ferracini, M. Bosetti, M. Prat, J. Gómez-Morales, Biomimetic citrate-coated luminescent apatite nanoplateforms for clofencin delivery in inflammatory environments, *Nanomater.* 12 (12) (2022) 562, <https://doi.org/10.3390/NANO12030562> (2022) 562.
- [75] J.R. Lakowicz, Principles of fluorescence spectroscopy, 2 nd. <https://doi.org/10.1007/978-0-387-46312-4>, 1999.
- [76] B. Dąbrowski, A. Żuchowska, Z. Brzócka, Graphene oxide internalization into mammalian cells – a review, *Colloids Surfaces B Biointerfaces* 221 (2023) 112998, <https://doi.org/10.1016/J.COLSURFB.2022.112998>.
- [77] H. Zhou, J. Lee, Nanoscale hydroxyapatite particles for bone tissue engineering, *Acta Biomater.* 7 (2011) 2769–2781, <https://doi.org/10.1016/J.ACTBIO.2011.03.019>.
- [78] J.W. Suk, R.D. Piner, J. An, R.S. Ruoff, Mechanical properties of monolayer graphene oxide, *ACS Nano* 4 (2010) 6557–6564, [https://doi.org/10.1021/NN101781V/SUPPL\\_FILE/NN101781V\\_SI\\_001.PDF](https://doi.org/10.1021/NN101781V/SUPPL_FILE/NN101781V_SI_001.PDF).
- [79] E. Butyrskaya, S. Zapryagaev, E. Izmailova, L. Nechaeva, Sorption interactions between l/d-alanine and carbon nanotubes in aqueous solutions, *J. Phys. Chem. C* 121 (2017) 20524–20531, [https://doi.org/10.1021/ACS.JPC.7B06849/ASSET/IMAGES/LARGE/JP-2017-06849M\\_0009.JPEG](https://doi.org/10.1021/ACS.JPC.7B06849/ASSET/IMAGES/LARGE/JP-2017-06849M_0009.JPEG).
- [80] M. Li, Y. Wang, Q. Liu, Q. Li, Y. Cheng, Y. Zheng, T. Xi, S. Wei, In situ synthesis and biocompatibility of nano hydroxyapatite on pristine and chitosan functionalized graphene oxide, *J. Mater. Chem. B* 1 (2013) 475–484, <https://doi.org/10.1039/c2tb00053a>.
- [81] M. Li, Q. Liu, Z. Jia, X. Xu, Y. Cheng, Y. Zheng, T. Xi, S. Wei, Graphene oxide/hydroxyapatite composite coatings fabricated by electrophoretic nanotechnology for biological applications, *Carbon* N. Y. 67 (2014) 185–197, <https://doi.org/10.1016/J.CARBON.2013.09.080>.
- [82] C. Song, C.M. Yang, X.F. Sun, P.F. Xia, J. Qin, B.B. Guo, S.G. Wang, Influences of graphene oxide on biofilm formation of gram-negative and gram-positive bacteria, *Environ. Sci. Pollut. Res.* 25 (2018) 2853–2860, <https://doi.org/10.1007/S11356-017-0616-8/FIGURES/5>.

- [83] M. Perkins, S.J. Ebbens, S. Hayes, C.J. Roberts, C.E. Madden, S.Y. Luk, N. Patel, Elastic modulus measurements from individual lactose particles using atomic force microscopy, *Int. J. Pharm.* 332 (2007) 168–175, <https://doi.org/10.1016/J.IJPHARM.2006.09.032>.
- [84] J.J. Roa, G. Oncins, J. Diaz, F. Sanz, M. Segarra, Calculation of young's modulus value by means of AFM, *Recent Pat. Nanotechnol.* 5 (2011) 27–36, <https://doi.org/10.2174/187221011794474985>.
- [85] W.R. Bowen, R.W. Lovitt, C.J. Wright, Application of atomic force microscopy to the study of micromechanical properties of biological materials, *Biotechnol. Lett.* 22 (2000) 893–903, <https://doi.org/10.1023/A:1005604028444/METRICS>.
- [86] Y. Liu, J. Huang, M. Niinomi, H. Li, Inhibited grain growth in hydroxyapatite-graphene nanocomposites during high temperature treatment and their enhanced mechanical properties, *Ceram. Int.* 42 (2016) 11248–11255, <https://doi.org/10.1016/J.CERAMINT.2016.04.038>.
- [87] L. Liu, J. Zhang, J. Zhao, F. Liu, Mechanical properties of graphene oxides, *Nanoscale* 4 (2012) 5910–5916, <https://doi.org/10.1039/C2NR31164J>.
- [88] E. Della Bella, A. Parrilli, A. Bigi, S. Panzavolta, S. Amadori, G. Giavaresi, L. Martini, V. Borsari, M. Fini, Osteoinductivity of nanostructured hydroxyapatite-functionalized gelatin modulated by human and endogenous mesenchymal stromal cells, *J. Biomed. Mater. Res., Part A* 106 (2018) 914–923, <https://doi.org/10.1002/JBM.A.36295>.
- [89] M.U. Munir, S. Salman, A. Ihsan, T. Elsamani, Synthesis, characterization, functionalization and bio-applications of hydroxyapatite nanomaterials: an overview, *Int. J. Nanomedicine*. 17 (2022) 1903–1925, <https://doi.org/10.2147/IJN.S360670>.
- [90] G. Turco, E. Marsich, F. Bellomo, S. Semeraro, I. Donati, F. Brun, M. Grandolfo, A. Accardo, S. Paoletti, Alginate/hydroxyapatite biocomposite for bone ingrowth: a trabecular structure with high and isotropic connectivity, *Biomacromolecules* 10 (2009) 1575–1583, [https://doi.org/10.1021/BM900154B/SUPPL\\_FILE/BM900154B\\_SI\\_001.PDF](https://doi.org/10.1021/BM900154B/SUPPL_FILE/BM900154B_SI_001.PDF).
- [91] X. Cai, H. Tong, X. Shen, W. Chen, J. Yan, J. Hu, Preparation and characterization of homogeneous chitosan-poly(lactic acid)/hydroxyapatite nanocomposite for bone tissue engineering and evaluation of its mechanical properties, *Acta Biomater.* 5 (2009) 2693–2703, <https://doi.org/10.1016/J.ACTBIO.2009.03.005>.
- [92] S.S. Silva, A.R.C. Duarte, J.M. Oliveira, J.F. Mano, R.L. Reis, Alternative methodology for chitin-hydroxyapatite composites using ionic liquids and supercritical fluid technology, *J. Bioact. Compat. Polym.* 28 (2013) 481–491, [https://doi.org/10.1177/0883911513501595/ASSET/IMAGES/LARGE/10.1177\\_0883911513501595-FIG6.JPEG](https://doi.org/10.1177/0883911513501595/ASSET/IMAGES/LARGE/10.1177_0883911513501595-FIG6.JPEG).
- [93] J. Prakash, D. Prema, K.S. Venkataprasanna, K. Balagangadharan, N. Selvamurugan, G.D. Venkatasubbu, Nanocomposite chitosan film containing graphene oxide/hydroxyapatite/gold for bone tissue engineering, *Int. J. Biol. Macromol.* 154 (2020) 62–71, <https://doi.org/10.1016/J.IJBIOMAC.2020.03.095>.
- [94] M. Mehrli, E. Moghaddam, S.F.S. Shirazi, S. Baradaran, M. Mehrli, S.T. Latibari, H.S.C. Metselaar, N.A. Kadri, K. Zandi, N.A.A. Osman, Mechanical and in vitro biological performance of graphene nanoplatelets reinforced calcium silicate composite, *PLoS One* 9 (2014) e106802, <https://doi.org/10.1371/JOURNAL.PONE.0106802>.
- [95] L. Sun, Z. Yan, Y. Duan, J. Zhang, B. Liu, Improvement of the mechanical, tribological and antibacterial properties of glass ionomer cements by fluorinated graphene, *Dent. Mater.* 34 (2018) e115–e127, <https://doi.org/10.1016/J.DENTAL.2018.02.006>.
- [96] C. Daulbayev, F. Sultanov, A.V. Korobeinyk, M. Yeleuov, A. Taurbekov, B. Bakbolat, A. Umirzakov, A. Baimenov, O. Daulbayev, Effect of graphene oxide/hydroxyapatite nanocomposite on osteogenic differentiation and antimicrobial activity, *Surface. Interfac.* 28 (2022) 101683, <https://doi.org/10.1016/J.SURFIN.2021.101683>.
- [97] J. Guo, G. Cao, S. Wei, Y. Han, P. Xu, Progress in the application of graphene and its derivatives to osteogenesis, *Heliyon* 9 (2023) e21872, <https://doi.org/10.1016/J.HELIYON.2023.E21872>.
- [98] Z. Liu, Y. Yu, W. Kang, F. Chen, F. Yan, B. Ma, S. Ge, Self-assembled terbium-amino acid nanoparticles as a model for terbium biosafety and bone repair ability assessment, *Compos. Part B Eng.* 244 (2022) 110186, <https://doi.org/10.1016/J.COMPOSITESB.2022.110186>.
- [99] B. Rahman, A.M. Deliormanli, H. Atmaca, Evaluation of in vitro bioactivity, cytotoxicity, and drug release behavior of Er<sub>2</sub>O<sub>3</sub> and Tb<sub>2</sub>O<sub>3</sub>-containing bioactive glass particles and nano fibers, *J. Inorg. Organomet. Polym.* 32 (2023) 3797–3812, <https://doi.org/10.1007/s10904-022-02373-2>.
- [100] N. Bellier, P. Baipaywad, N. Ryu, J.Y. Lee, H. Park, Recent biomedical advancements in graphene oxide- and reduced graphene oxide-based nanocomposite nanocarriers, *Biomater. Res.* 26 (2022) 65, <https://doi.org/10.1186/s40824-022-00313-2>.
- [101] J. Zhang, H.Y. Cao, J.Q. Wang, G.D. Wu, L. Wang, Graphene oxide and reduced graphene oxide exhibit cardiotoxicity through the regulation of lipid peroxidation, oxidative stress, and mitochondrial dysfunction, *Front. Cell Dev. Biol.* 9 (2021) 616888, <https://doi.org/10.3389/fcell.2021.616888>.